19. Analysis and Correlation of Volcanic Ash in Marine Sediments from the Peru Margin, Ocean Drilling Program Leg 201: Explosive Volcanic Cycles of the North-Central Andes[1]

D. Hart[2] and D.J. Miller[3]

ABSTRACT

Although land studies have identified major volcanic centers of historic eruptions within the Central Andes, the tephrachronologic record is disturbed by the high erosion rates in this arid region. Owing to erosion, studies of volcanic cyclicity based on subaerial deposits offer an incomplete record of the frequency and episodicity of eruptions since the Miocene. However, volcanic material commonly occurs in marine sediment as discrete ash fall layers and/or disseminated ash accumulations. A detailed investigation of cores from three sites offshore Peru drilled during Ocean Drilling Program (ODP) Leg 201 has been conducted to determine the occurrence of volcanic ash layers and ash accumulations within marine sediments along the Peru shelf. These sites were previously occupied during ODP Leg 112, which suffered from poor and/or disturbed core recovery. Advancements in hydraulic piston coring realized since and employed during Leg 201 resulted in better core recovery and less disturbance of sediment throughout the cored intervals. Because marine sediments potentially undergo less erosion than land deposits and because Leg 201 benefited from improved recovery of less disturbed cores, the tephrachronologic record from Leg 201 yielded a more complete record of explosive activity for north-central Andean volcanism than previous studies. Ash layers were identified through detailed core descriptions supplemented by smear slide analysis. Primary

ash layers were confirmed through whole-rock and glass geochemistry and petrographic analyses. These data also provided information concerning volcanic episodes represented by the ash layers through correlation to land studies. In addition, correlative ties between drilling sites are suggested. The improved recovery enabled the detailed examination of cores from the Peru margin needed to test the hypothesis that volcanic ash layers and accumulations are more abundant in the study region than previously reported.

INTRODUCTION

Volcanic material commonly occurs in marine sediment as discrete ash fall-out layers and/or disseminated ash accumulations within sediment deposits. Ash layers are useful indicators of explosive eruption cycles and can be used to calculate the approximate magnitude and duration of an eruption (Shane, 2000; Pattan et al., 1999; de Silva and Zielinski, 1998; Lackschewitz and Wallrabe-Adams, 1997; Ledbetter and Sparks, 1979). In order to determine the occurrence of volcanic ash layers and accumulations within marine sediment along the Peru shelf, detailed examination of cores from three Peru margin sites (Fig. F1) cored during Ocean Drilling Program (ODP) Leg 201 was conducted.

Pouclet et al. (1990) determined the presence of volcanic ash layers and accumulations in Quaternary to late Eocene sediments from cores drilled along the Peru shelf during ODP Leg 112. They report a total of 30 ash layers, with the predominant amount of ash (8 layers: ~84 cm of ash deposited) present at their southernmost site; the reported ash layers are restricted to the upper portion of the cored sections because the lower portion experienced poor recovery. Three (Sites 684, 680, and 681; Fig. F1) of the eight sites studied during Leg 112 were reoccupied during Leg 201 (northern transect Site 1227 and southern transect Sites 1228 and 1229, respectively). From Sites 680, 681, and 684, six ash layers, one ash pod, and eight ash-bearing layers were reported (Pouclet et al., 1990).

Pouclet et al. (1990) estimated explosive activity in relation to time along the Andean arc for the past 35 m.y. through petrographic and chemical analyses coupled with examination of the geographical and chronological distributions of the ash layers. Their data suggest that the record of explosive activity starts in the late Eocene (~35 Ma) and continues into the Holocene, with the bulk of activity occurring during the late Miocene (10–8 Ma) and Pliocene. However, the tephrachronologic record of Pouclet et al. (1990) may be incomplete because of the use of rotary coring techniques (extended core barrel [XCB] and rotary coring barrel [RCB]) of the lower portion of the cored sections, leading to poor recovery of these deeper sections. Advanced piston coring (APC) was used to drill the upper portion of the cored sections, returning near-complete recovery and only slightly disturbed cores (Suess, von Huene, et al., 1990).

Advancements in APC techniques employed during Leg 201 resulted in better core recovery and less disturbance of sediment throughout the entire cored sections (Table T1; for an explanation of drilling techniques, see D'Hondt, Jørgensen, Miller, et al., 2003), allowing a more complete sedimentological analysis of the region. The Leg 201 *Initial Reports* volume (D'Hondt, Jørgensen, Miller, et al., 2003) suggests abundant ash layers throughout core sections from Hole 1228A that are not reported in corresponding sections from Site 680.

F1. CVZ, land studies, and Leg 34, 112, and 201 sites, p. 20.
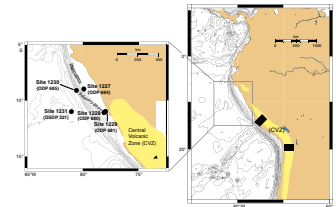
T1. Leg 112 and 201 core recoveries, p. 33.

Detailed core descriptions and petrographic study of smear slides and grain mounts from Leg 201 sites have been carried out in order to determine the presence of ash accumulations within the marine sediment along the Peru shelf. Ash layers have been characterized through whole-rock geochemical analysis. This study built upon the preliminary results from Leg 201 shipboard core descriptions, which describe numerous ash layers that were not reported in the corresponding Leg 112 sites. This study has resulted in a more complete record of ash-bearing intervals (intervals are based on shipboard lithostratigraphic horizons and biostratigraphic dates) in the cores from the Peru margin. These data complement land-based tephrachronologic studies and contribute to a better understanding of the episodicity of explosive volcanic activity in the Central Andes.

GEOLOGIC SETTING

Subduction of the oceanic Nazca plate beneath the continental South American plate is responsible for the formation and volcanic processes of the Andes along the western edge of South America (Thorpe and Francis, 1979). Three linear zones of active volcanism are present along the Andean Cordillera (Fig. F2): the northern volcanic zone (NVZ: 5°N–2°S) in Columbia and Ecuador, the central volcanic zone (CVZ: 16°–28°S), primarily in south Peru and north Chile but extending easterly into southwestern Bolivia and northwestern Argentina, and the southern volcanic zone (SVZ: 33°–52°S), primarily in southern Chile and southern Argentina (Thorpe and Francis, 1979; Baker and Francis, 1978; de Silva and Francis, 1991).

The Altiplano of Bolivia and the Puna of northern Chile and Argentina dominate the CVZ (de Silva and Francis, 1991). These high plateaus, with elevations >4000 m, separate a double mountain chain (the Western [Occidental] and Eastern [Oriental] Cordilleras; Fig. F2) in which the peaks are largely constructed of andesitic composite volcanoes (de Silva and Francis, 1991; Baker and Francis, 1978). Upper Cenozoic ignimbrite sheets are widespread along the western flanks of the Western Cordillera and the Altiplano and reach parts of the Eastern Cordillera (Fig. F2). These large ignimbrite sheets are also present within the Western Cordillera (Baker and Francis, 1978; de Silva, 1989; Francis and Baker, 1978; Baker, 1981; Sparks et al., 1985; de Silva and Francis, 1989). The Western Cordillera experienced the bulk of volcanic activity in this upper Cenozoic volcanic region; however, a few unique events occurred in the Eastern Cordillera in Bolivia (de Silva and Francis, 1991; Baker and Francis, 1978).

The large-magnitude eruptions that deposited the extensive ignimbrite sheets along the western flanks of the Western Cordillera may also be responsible for the marine ash layers deposited in the study region because "an unknown, and possibly large, proportion of the erupted material would have been dispersed as fine-grained air-borne ash" (Baker and Francis, 1978). The ash layers discussed in this paper are believed to have erupted from volcanic centers of the CVZ and were transported west-northwestward into the study region by south–southeast winds and ocean currents (Fig. F3) (Garcia, 1994; Thouret et al., 1997, 2002; de Silva and Zielinski, 1998).

F2. Volcanic zones of the Andes and areal exposure of Cenozoic–Holocene volcanics, p. 21.
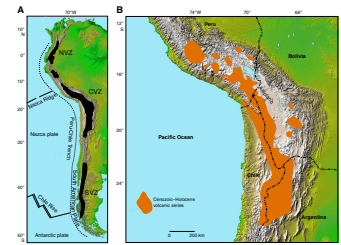
F3. Flow paths of major ocean currents around South America, p. 22.
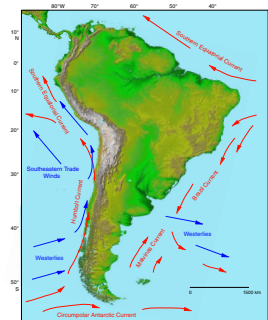
PREVIOUS WORK

Marine Studies

Volcanic ash layers, pods, and dispersed glass were observed in Quaternary to upper Eocene sediment in cores drilled off Peru during Leg 112 (Pouclet et al., 1990). Pouclet et al. (1990) collected 41 samples containing volcanic material from these cores. Of the 41 samples, only 4 were from the three sites reoccupied during Leg 201 (Leg 112 Sites 684, 680, and 681; Leg 201 Sites 1227, 1228, and 1229, respectively). Of these four samples, three were ash layers (one ash layer from each of Sites 684, 680, and 681) and one was from an ash pod (a lenticular to cylindrical ash accumulation that pinches out within the diameter of the core) from Site 680. In addition to these sampled ash layers and pod, Pouclet et al. (1990) report an ash pod from Site 684, eight ash-bearing beds (1–5 cm thick) from Site 680, and several occurrences of dispersed ashy material within several sections of core from all three sites. The ash from Leg 112 sites has predominantly medium to high potassium (andesitic and shoshonitic), calc-alkalic, dacitic to rhyolitic compositions, with the exception of 8 of the 41 samples analyzed that have andesitic compositions, and no samples have low potassium (Pouclet et al., 1990). These data coupled with analyses of the geographical and chronological distributions allowed Pouclet et al. (1990) to interpret the origin of volcanic material to be from the Andean volcanic arc and to estimate explosive activity in the region in relation to time along the Andean arc for the past 35 m.y. Their study suggests that explosive activity began in the late Eocene (reports of sparse ash layers at ~35 Ma) in the northern region (Sites 683, 684, and 685). Activity continued with two pulses during each of three Miocene series (late, middle, and early Miocene). No ash layers were reported for the Pliocene; however, two ash layers have been reported from the Pleistocene and Pleistocene-Holocene sections. Based on the samples collected during ODP Leg 112, Pouclet et al. (1990) interpret that greatest explosive activity occurred during the late Miocene for the northern region, with eight ash layers depositing a cumulative total of ~28 cm of ash deposited at these sites from 10 to 8 Ma.

Preserved ash layers suggest there was explosive volcanic activity during the late Miocene in the southern part of the Leg 112 study area (Sites 679, 680, and 681) that continued through the Holocene. The early and middle Miocene sediments record one volcanic pulse each (16.5–15.5 Ma and 13.5–12.5 Ma, respectively), and at least seven ash layers were deposited during each series; the total thickness of these ash layers for each pulse was reported as ~17.5 cm (Pouclet et al., 1990). Apparent activity increased to two pulses until the Pleistocene–Holocene. The Pliocene marked a time of relatively intense activity, with at least seven ash layers, representing as much as 60 cm of material between 5–4 Ma and 4–1.5 Ma. The record of volcanism is sparser through the Pleistocene section. Only two pulses (1.5–1 Ma and 1–0.5 Ma) of activity occurred and three ash layers were preserved with a cumulative thickness of ~3.5 cm of ash. Activity evidently picked up once again during the Pleistocene–Holocene with one volcanic pulse at 0.5 Ma that produced at least five ash layers representing ~20 cm of ash (Pouclet et al., 1990).

Vigorous volcanic activity recorded in the sediments from the southernmost sites (Sites 686 and 687—not reoccupied during Leg 201) occurred from the Pliocene through the Pleistocene–Holocene. One large

pulse of activity is recorded in Pliocene sediments (2–1.65 Ma) indicated by least three ash layers with a cumulative thickness of ~14 cm. This activity continued into the Pleistocene with two more large pulses (1.65–1 Ma and 1–0.5 Ma), and six ash layers reported with a cumulative thickness of 32 cm. The Pleistocene–Holocene is marked by one more large pulse (0.5–0 Ma) of volcanism, with five ash layers preserved with a cumulative thickness of 22.5 cm (Pouclet et al., 1990). These southernmost sites are evidence of a time of intense volcanism within the CVZ, with a cumulative thickness of 68.5 cm of volcanic ash preserved at both sites.

This record of explosive volcanic activity reported by Pouclet et al. (1990) depicts variations in eruption cycles between the northern and southern sites of Leg 112. They report intense volcanic episodes during the Pliocene–Quaternary at the southern sites that are not recorded at the northern sites. For example, they report up to 74 cm of tephra per 0.5 m.y. in the upper Pliocene at the southern sites, and no tephra deposits are recorded at all within the Pliocene sediments of the northern sites. In addition, they report a sizeable decrease in explosive activity throughout the Pleistocene and Pleistocene–Holocene (~2 cm total of ash total measured for both periods) for the northern sites, whereas these time sections yield a large amount of tephra (~93 cm) at the southern sites, indicating an increase of explosive activity for this region. Pouclet et al. (1990) assign this variation to the seismic gap of the northern Peruvian Andes located between 3° and 16°S latitude.

Another area that was investigated prior to Leg 201 that was reoccupied as Site 1231 was a location spot cored during the Deep Sea Drilling Project (DSDP) during Leg 34 as Site 321. This location is west of the Peru-Chile Trench. No ash layers were reported from sediments recovered at this site during Leg 34, but Donnelly (1976) estimated accretion rates of volcanic material along the Peru margin over the past 10 m.y. from spot samples containing dispersed volcanic constituents from this site. He reports that the upper Miocene to present sediments record moderate amounts of volcanic activity during these time periods. The age and chronology of volcanic debris for both studies were determined using estimated sedimentation rates established from biostratigraphy (Suess, von Huene, et al., 1990; Yeats, Hart, et al., 1976).

Land Studies

The CVZ of the Central Andes is one of the largest volcanically active regions of the world (de Silva and Francis, 1991; Francis and de Silva, 1989). The principal magma source for the andesitic volcanoes of the CVZ is believed to be derived from partial melting of an asthenospheric wedge between the overriding continental South American plate and the descending oceanic Nazca plate (Fig. F2) (de Silva and Francis, 1991; Thorpe and Francis, 1979; Baker and Francis, 1978; Hanus and Vanek, 1978). This magma source produced Upper Cretaceous (Aptian stage, 114–108 Ma) through Quaternary subaerial volcanic sequences of andesite, basalt andesite, and rhyolite to rhyodacite lavas, tuffs, and volcaniclastics that were deposited throughout the Central Andes (Lindsay et al., 2001; de Silva, 1989; de Silva and Francis, 1989; Sparks et al., 1985; Hall and Calle, 1982; Lahesen, 1982; Baker, 1981; Tosdal et al., 1981; Baker and Francis, 1978; Francis and Baker, 1978; Noble et al., 1974). Detailed studies of these deposits have been conducted by combining field data and Landsat (Thematic Mapper) images. These studies have reported ash flow tuff and ignimbrite deposits covering large areas

of the CVZ and having volumes of several hundred cubic kilometers (Lindsay et al., 2001; de Silva and Francis, 1989; Baker and Francis, 1978). Ash fall covering an area of 300,000 km² with an approximate volume of 8.8 km³ (combined air fall ash and pyroclastic material has a volume of 19.2 km³) has been documented for one historically large eruption, that of Huaynaputina located at 16°35′S, 70°52′W in southern Peru (the northernmost portion of the CVZ) (Adams et al., 2001; de Silva and Zielinski, 1998) (Fig. F1). This eruption has been described as the largest historic eruption of the Andes with ash fall deposits as thick as 5 cm at a distance 200 km away from the source (Adams et al., 2001).

Intense volcanic activity during the middle to late Miocene and into the Pliocene followed the reinception of volcanic activity along the CVZ during the early Miocene (Noble et al., 1974; Baker and Francis, 1978; Tosdal et al., 1981; Lahesen, 1982). A thick layer of tuff and lava from this active zone was believed to blanket a large part of the Central Andes during this time (Noble et al., 1974). Baker and Francis (1978) as well as other authors (de Silva, 1989; Francis and Baker, 1978; Baker, 1981; Tosdal et al., 1981; de Silva and Francis, 1989; Sparks et al., 1985) documented the existence of large dacitic and rhyodacitic ignimbrites, some covering areas in excess of 2300 km² in the Central Andes (Francis and Baker, 1978). Although these formations may cover large areas of the Andes, lavas (typically andesitic) still dominated the region volumetrically into the Pliocene (Baker and Francis, 1978); however, in local areas ignimbrites dominate the volcaniclastic stratigraphy in volume and area (de Silva, 1989). The general agreement among authors is that these extensive ignimbrite eruptions began during the late Miocene and continued into the Pliocene, which is concurrent with the eruption periods from the marine studies of Pouclet et al. (1990). A large number of small and large stratovolcanoes formed along the Cordillera Occidental of southern Peru and northern Chile in the early Pliocene with the progression of voluminous calc-alkaline, intermediate lava flows (Tosdal et al., 1981; Lahesen, 1982). These andesitic flows succeeded the large-volume ignimbrite eruptions from the late Pliocene through the Quaternary (Tosdal et al., 1981; Baker and Francis, 1978). A number of large stratovolcanoes that initially developed during the Pleistocene accommodated Holocene volcanism in the CVZ (Tosdal et al., 1981).

Baker and Francis (1978) revealed regional variations in volcanic episodicity within the northern (19°30′–21°S) and southern (21°–22°30′S) parts of the central portion (19°30′–22°30′S) of the CVZ. In the northern portion of their study area two periods of peak activity occurred, one during the middle Miocene and the other from late Miocene to early Pliocene, whereas in the southern region of their study area the largest volume of volcanic material was erupted from the late Miocene to Holocene. The largest volume of ignimbrites (650 km³) was deposited during the early Miocene. In addition, Baker and Francis (1978) record two more deposits of 150 km³ each (one during the late Miocene and one during the late Miocene to early Pliocene), one deposit of 75 km³ (early Pliocene–Holocene), and one deposit of 50 km³ (middle Miocene) for their northern region. In their southern region, Baker and Francis (1978) report ignimbrite eruptions beginning during the middle Miocene with the largest deposits occurring within the late Miocene–early Pliocene, depositing 500 km³ of material. In addition, two deposits of 250 km³ were recorded during the middle Miocene and early Pliocene to Holocene and one deposit of 200 km³ was deposited during the late Miocene (Baker and Francis, 1978). These large ignimbrite deposits are

of the most significance when correlating marine ash (air fall) layers with land studies because they provide evidence of the occurrence of airborne ash (Baker and Francis, 1978) and of large plinian-style eruptions, which can produce a significant amount of air fall ash (Fisher and Schmincke, 1984). Tosdal et al. (1981) performed a geochronology of southern Peru (the northernmost region of the CVZ) pertaining to upper Cenozoic (Miocene–Holocene) volcanic rocks. Their record indicates five separate rhyodacite ignimbrite formations in which eruptive episodes began in the late Oligocene and continued through the Miocene and into the earliest Pliocene. Andesite and dacite lava flows predominated throughout the Pliocene (Tosdal et al., 1981). The record of eruption cycles in Tosdal et al. (1981) best matches that of Baker and Francis's (1978) northern region, with most ignimbrites being deposited during the late Miocene.

METHODS

Five holes were drilled during Leg 201 at each of Sites 1227, 1228, and 1229 (D'Hondt, Jørgensen, Miller, et al., 2003). Cores from the initial hole (A) of each site were chosen for examination during this study because this hole obtained the deepest penetration (150.51, 200.9, and 194.4 meters below seafloor [mbsf], respectively) at each site and the greatest average recovery of sediment (66.5%, 68%, and 44%, respectively). Recovery was 100% in upper half of hole A at each site (D'Hondt, Jørgensen, Miller, et al., 2003).

The frequency and curated depths of ash layers and accumulations were documented by relogging the cores at the Integrated Ocean Drilling Program (IODP) Gulf Coast Repository at Texas A&M University. The occurrence of ash layers and accumulations was determined through detailed visual core and smear slide analyses, and ages were inferred from the biostratigraphy of corresponding Leg 112 sites.

Sixty-eight bulk ash samples from distinct layers were sent to a commercial industrial laboratory (Acme Analytical Laboratories) for inductively coupled plasma (ICP) analysis for major element oxides, trace elements, and rare earth elements (REE; whole-rock compositions were determined through ICP-atomic emission spectroscopy [AES] and ICP-mass spectrometry [MS] analyses). Precision and reproducibility of the results were evaluated, respectively, through the use of U.S. Geological Survey (USGS) standard reference materials submitted for analysis as unknowns and duplicates. A second portion of the sampled ash layers was passed through a 63-µm sieve to remove clay-sized particles. Grain mounts were prepared with grains ≥63 µm. Major and minor elements were determined for glasses from each grain mount using the Texas A&M Cameca SX-50 automated electron microprobe, equipped with auto focus, an optically encoded stage, and extensive Sun workstation–based image processing capabilities. These analyses were run with the following operating parameters: accelerating voltage = 15 kV, sample current = 10 nA, beam diameter = 10–12 µm, and count time = 20–40 s. Five glass standards (one Yellowstone glass, one tektite, and three basaltic glasses) were used for calibration, and standard checks were run once on all five glasses and three times on the Yellowstone glass to test for precision and reproducibility of the analyses. These data were used to confirm the origin of Leg 201 ash content and to classify and correlate ash layers.

RESULTS

Leg 201 sediments consist of interbedded diatom, foraminifer, and nannofossil oozes (Suess, von Huene, et al., 1990). These beds are olive-green, dark green, brown, or black with yellow-tan laminae and range in grain size from clay to sand. Volcanic ash layers, laminae, and/or accumulations are also present within cores from all three sites (Table T2). Volcanogenic deposits are abundant within cores from Sites 1228 and 1229 and are dispersed throughout most of the cores at these sites. These deposits are scarce at Site 1227 and are restricted to the upper and lower three cores (Cores 201-1227A-1H through 3H and 11H through 13H, respectively) at this site.

Some ash layers were easy to recognize during the visual examination of cores because of their strong color contrast to biogenic sediments (gray, tan-gray and black, and cream), whereas others were darker in color (black or brown) and resemble biogenic beds. The ash layers in this study tend to be coarser grained than the biogenic material above and below them, signifying a change in lithology. This change in lithology aided in the distinction between darker ash layers and biogenic sediments.

Ash Layer Description

Ash layer contacts are primarily sharp with rare gradational contacts. Three layers from Hole 1228A and five layers from Hole 1229A are normally graded; the rest are either homogeneous or slightly graded. The ash layers present at each site are described in Table T3. Figure F4 displays a representative ash layer sample from each site. Ash layers and accumulations have been categorized in four groups based on the percent biogenic material or diagenesis present. The petrographic criteria for selecting Type 1 ashes were that these layers contain (1) ≤5% biogenic component and (2) ≤1%–2% rounded grains. Additionally, all Type 1 ash layers were required to possess either (1) a high abundance (≥10%) of glass/pumice or (2) glass/pumice (1%–2%) and at least 0.5%–1% amphibole or biotite. Ash layers that met these criteria were sampled for whole-rock geochemical analysis. Type 2 ash occurrences contain biogenic or dolomite content >20% but <60%; Type 3 ash occurrences contain >60% biogenic material, and Type 4 ash occurrences contain >60% dolomite. Some Type 4 ash layers might have been Type 1 prior to diagenesis. Type 2 through Type 4 ash occurrences are recorded in Table T4, and all ash content is summarized below. Because we elected to establish an arbitrary boundary for nonvolcanic components to define the limit of ash layer type, we adopt the term borderline ash accumulations for those samples that are within the error of visual estimate of content (±2%–3%).

Site 1227 Ash Layers

Site 1227 is located on the upper slope of the southeastern edge of the Trujillo Basin (Fig. F1) at a water depth of 427.5 m (D'Hondt, Jørgensen, Miller, et al., 2003; Pouclet et al., 1990). The cores from this site contain one Type 1 ash layer (1.3 cm), two Type 2 layers (0.5 and 1.3 cm), and nine Type 3 layers (Table T4). In addition to these layers and accumulations, 12 Type 4 layers have been recognized. Type 1 ash layers for this hole consists of ~85%–90% volcanic glass with 5%–10% quartz and feldspar (no mafic minerals are present), and there is no

rounding of grains and little or no biogenic component present (Fig. F4; Table T3). According to the stratigraphic section (Fig. F5), this layer occurs in Miocene sediments, whereas the two Type 2 layers occur in Pliocene sediments. Type 3 ash occurs predominantly within Pleistocene sediments and within one Holocene, one Pliocene, and two Miocene layers as well. Type 4 ash layers occur within Pliocene and Miocene sediments with the exception of one Holocene layer.
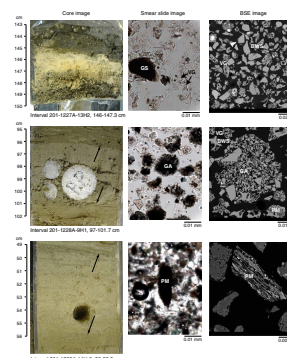
Site 1228 Ash Layers

Site 1228 is located on the Peru shelf at the southeastern edge of the Salaverry Basin (Fig. F1) at a water depth of 252 m (D'Hondt, Jørgensen, Miller, et al., 2003; Pouclet et al., 1990). The cores from this site contain 52 Type 1 ash layers, 38 of which were analyzed for whole-rock geochemistry (layer thickness ranges from 0.5 to 13.5 cm) (Table T3), and 28 Type 2 ash layers, 8 of which contain some dolomite (layer thickness ranges from 0.7 to 14 cm). Layers containing Type 3 ash are dispersed throughout the entire Pleistocene–Pliocene cored sections. In addition, 11 Type 4 layers are present in Cores 201-1228A-5H through 9H (Table T4). Type 1 ash layers from this site consist mostly of quartz and feldspars (usually 85%–90%, varying between quartz and feldspar) and contain, on average, 0%–2% mafic, pleochroic minerals (biotite or hornblende) and 0%–5% volcanic glass. Seven of the Type 1 layers have no round quartz; two contain 50% and 70% volcanic glass, four contain high pumice (40%–80%), and one contains low glass and pumice (Fig. F4; Table T3). These Type 1 ash layers are shown in the stratigraphic section (Fig. F5) as occurring within Pliocene sediments, whereas Type 2 ash layers occur within Holocene, Pleistocene, and Pliocene sediments, Type 3 and Type 4 ashes occur within Pleistocene and Pliocene sediments.

Site 1229 Ash Layers

Site 1229 is located on the Peru shelf at the southeastern edge of the Salaverry Basin slightly northwest of Site 1228 (Fig. F1) (D'Hondt, Jørgensen, Miller, et al., 2003; Pouclet et al., 1990). This site is the most landward site of the three sites in this study region and was drilled at a water depth of 150.5 m (D'Hondt, Jørgensen, Miller, et al., 2003). The cores from this site contain 15 Type 1 ash layers, 8 of which are considered borderline and 14 of which were analyzed for whole-rock geochemistry. In addition, there are 6 ash laminae of Type 1 composition (Table T3) and 92 Type 2 ash layers (9 pods, 1 lens, and 1 laminae set), 24 Type 3 ash occurrences (2 pods), and 23 Type 4 layers that contain varying amounts of dolomite (3 are borderline) (Table T4). Type 1 ash layers for this site consist mostly of quartz and feldspars (usually 85%–92% varying between quartz and feldspar) and contain, on average, 0%–2% mafic, pleochroic minerals (biotite or hornblende), and 0%–3% volcanic glass (Table T3; Fig. F4). These Type 1 ash layers are shown in the stratigraphic section (Fig. F5) as occurring within Pleistocene and Pliocene sediments, whereas Type 2 ash layers occur within Holocene, Pleistocene, and Pliocene sediments and Type 4 layers occur within Pleistocene sediments (with the exception of one layer in interval 201-1229A-18H-2, 127–128.8 cm [~138.4 mbsf] that occurs just below the Pleistocene/Pliocene boundary).
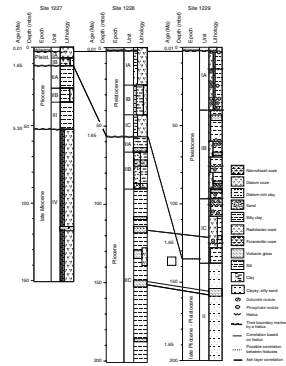
Glass Geochemistry of Type 1 Ash Layers

Geochemical analysis of glass shards was conducted on a select group of ash layers from each Leg 201 site. We attempted to analyze at least 10 glass shards from each ash layer; however, fewer analyses were conducted for some layers because of the very fine grained nature of some samples and the plucking of grains during polishing of the microprobe mounts. The results of these analyses are displayed on total alkalis vs. silica (TAS) and potassium vs. silica plots (Figs. F6, F7) for both the full set of glasses analyzed and the average value for each ash layer, respectively.

Overall, Leg 201 glasses display predominantly rhyolitic (–70 wt% SiO_2) chemical compositions (Table T5) and plot mostly in the subalkaline (tholeiitic) series on a TAS diagram (Fig. F6). However, two samples have andesitic compositions (most likely due to hydration of glass, indicated by low total values), four samples have trachyte–trachydacitic compositions, and one sample has a dacitic composition (Fig. F6; Table T5). Additionally, the dacitic sample and one other sample (which falls on the boundary between dacite and rhyolite) have very low alkali contents (<4 wt%) and two of the rhyolitic samples have very high silica values (>80 wt%).

Average glass compositions form two distinct groupings in TAS space. Five samples from Hole 1228A have total alkali of 8.33–8.56 wt% and SiO_2 of 69.8–71.6 wt%. We designate these samples geochemical Group 1, whereas the remaining four Hole 1228A samples and all Hole 1227A and 1229A samples (geochemical Group 2) have lower total alkalis (7.29–8.06 wt%) and higher silica (72.9–74.2 wt%). One exception is a Hole 1228A sample that has elevated SiO_2 (81.3 wt%) and may not reflect a primary ash composition (Table T5; Fig. F7).

On average, the rhyolitic glasses plot in the high-K calc-alkaline and shoshonite fields in the K_2O vs. SiO_2 space (Figs. F6, F7), which complements the Pouclet et al. (1990) geochemical evaluation of glasses from the same region (Leg 112). The average values for the most representative major element oxides are plotted against silica and their trends are displayed on variation diagrams in Figure F8. Additionally, major element oxide regions for glass values from Leg 112, the CVZ, and offshore Central America are included on the variation diagrams for the purpose of possible source region comparisons.

Major element data for glasses within Group 1 display clear and almost linear trends with increasing CaO and K_2O and decreasing FeO, Na_2O, TiO_2, and MgO (which is not quite as distinct as most of the trends) as SiO_2 increases. Major element data for glasses in Group 2 do not display clear linear trends with increasing SiO_2 content. The data for these glasses tend to cluster around one particular value as SiO_2 increases per major element oxide (Fig. F9). Additionally, the data for this group can be further subdivided into two separate groups for Al_2O_3, CaO, MgO, and Na_2O, with each grouping around one value per major element oxide with increasing SiO_2.

All Leg 201 glasses have major element oxide values that plot on variation diagrams (Fig. F9) within the range of Leg 112 samples, with the exception of the one sample from Hole 1228A that has elevated SiO_2. Most major element oxide data also fall within the CVZ region with the exception of Al_2O_3 (Fig. F8). All Leg 201 glass values plot outside the Central American region, with the exception of Na_2O and K_2O, in which a minimal number plot within this region.

F6. TAS vs. silica and potassium vs. silica for glass, p. 25.
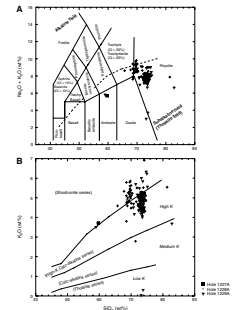
F7. TAS and potassium vs. silica for glass, p. 26.
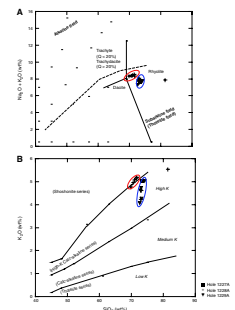
T5. Average glass analyses, p. 39.

F8. Major element oxides from glass analysis, p. 27.
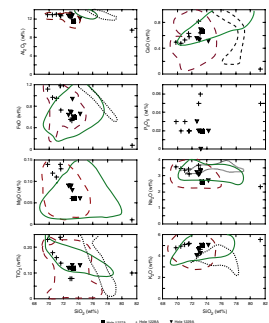
F9. TAS and potassium vs. silica for whole-rock analyses, p. 28.
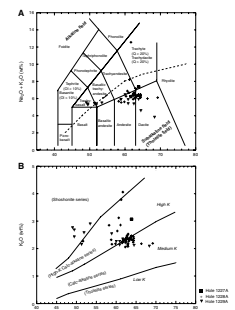
Whole-Rock Geochemical Analysis

Major Element Oxides

Leg 201 ash layers have predominantly andesitic to dacitic (58.8 < SiO_2 < 64.5 wt%) whole-rock chemical compositions (Table T6) and plot in the subalkaline (tholeiitic) series in TAS space (Fig. F9). However, seven samples have trachybasaltic to basaltic trachyandesitic (49.5 < SiO_2 < 53.5 wt%) compositions. These values are most likely low due to hydration evidenced by the relatively high (>10 wt%) loss on ignition (LOI) values (Fig. F9). Four of the dacitic samples are distinguished from the rest, in that two of them have high silica values (66.4 and 69.2 wt%) and the other two have the lowest total alkali values (3.79 and 4.55 wt%) (these low values are due to low sodium values, 1.71 and 2.44 wt%, respectively) (Fig. F9). The Hole 1229A sample with the lowest sodium has a high concentration of silica (68.4 wt%) as well. Additionally, six samples with average silica values lie on or just above the boundary between the trachyandesite/trachydacite fields and andesite-dacite fields (one sample from Hole 1227A plots well within the trachyandesite field). All ash layer samples have whole-rock compositions that fall in the medium-K or high-K calc-alkaline fields, with the exception of the seven hydrated samples discussed above (Fig. F9).

Whole-rock major element oxide data are plotted vs. silica in Figure F10. Additionally, major element oxide regions for whole-rock values from the CVZ, the NVZ, and the SVZ are included on the variation diagrams for the purpose of possible source region comparisons.

The hydrated ash layers plot to the left side (low silica) on the variation diagrams. The intermediate (andesitic and trachyandesitic) and acidic (dacitic and trachytic) samples plot together and display regular and continuous trends with increasing Al_2O_3, Na_2O, K_2O, and TiO_2, as SiO_2 increases for Hole 1228A samples. These element oxides decrease with increasing SiO_2 for Hole 1229A samples, with the exception of TiO_2, for which a trend is unapparent. CaO, Fe_2O_3, and MgO decrease as SiO_2 increases for samples from both sites; apparent trends are less obvious for P_2O_5 with increasing SiO_2.

Samples from Holes 1228A and 1229A have P_2O_5 values between 0.12 and 2.65 wt% and 0.10 and 1.36 wt%, respectively (average values = 1.09 and 0.49 wt%, respectively), which in some samples is considerably greater than that reported by the USGS and Le Maitre (1976) for andesitic to dacitic whole-rock standard compositions (0.15–0.63 wt%). The high P_2O_5 values for these samples can possibly be attributed to diagenetic alteration, in the form of secondary apatite and phosphate, since fluoroapatite and phosphate concretions have been documented throughout Leg 201 cores (D'Hondt, Jørgensen, Miller, et al., 2003).

Nearly all Leg 201 samples (with the exception of the hydrated rocks) have major element oxide values that plot within the field of published CVZ values (Fig. F10) within the CVZ region. One sample from Hole 1228A plots outside of the CVZ region for Al_2O_3 and Na_2O, one Hole 1229A sample plots outside the CVZ field for Fe_2O_3, Na_2O, and TiO_2. The Hole 1227A sample plots outside the CVZ array for TiO_2. The NVZ region overlaps that of the CVZ for all major element oxides with the exception of Fe_2O_3 and MgO (Fig. F10).
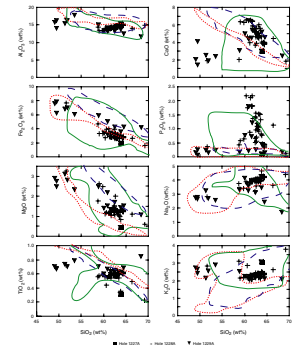
Rare Earth Elements

Chondrite-normalized rare earth element (REE) plots for Andean volcanic zones and for all Type 1 ash layers are shown in Figure **F11.** The REE pattern for most ash layers steadily decreases from the light REE (LREE) to middle REE (MREE). Heavy REE (HREE) displays a nearly flat pattern (Fig. **F11**). These REE patterns are most similar to those of the CVZ (Fig. **F11**). REE of the SVZ and NVZ are more HREE enriched and thus display a less steeply sloping pattern (Fig. **F11**). Based on these data our samples have more of an affinity to CVZ type ashes than SVZ and NVZ.

Two ash layers, one from Site 1227 and one from Site 1228, display REE patterns that are anomalous. These layers display steeply sloping REE patterns, and the layer from Site 1228 is slightly more enriched in HREE than the layer from Site 1227 (Fig. **F11**).

REE patterns are commonly used to indicate processes occurring during magma generation (Richards and Villeneuve, 2001; Monzier et al., 1999; Trumbull et al., 1999; Droux and Delaloye, 1996; Matteini et al., 2002; Dorendorf et al., 2000; Rollinson, 1993). As previously noted, the principal magma source for the andesitic volcanoes of the CVZ is interpreted to be partial melting of an asthenospheric wedge between the overriding continental South American plate and the descending oceanic Nazca plate (de Silva and Francis, 1991; Thorpe and Francis, 1979; Baker and Francis, 1978; Hanus and Vanek, 1978). The moderate depletion of HREE with respect to LREE displayed by all Leg 201 ash layers (Fig. **F11**) indicates either partial melting of a lower crust or mantle source region with garnet as a residual phase or precipitation of garnet in a deep-seated magma body (Richards and Villeneuve, 2001; Monzier et al., 1999; Trumbull et al., 1999; Droux and Delaloye, 1996; Matteini et al., 2002; Dorendorf et al., 2000; Rollinson, 1993). The suppressed negative Eu anomaly (with respect to CVZ samples) could be due to effective plagioclase enrichment in the ashes owing to winnowing of more dense ferromagnesian phases during airborne transport. However, the occurrence of Eu as Eu^{3+} has been noted by Richards and Villeneuve (2001) to frequently occur within fairly oxidized and hydrous arc magmas, resulting in a weak or lacking negative Eu anomaly as well. The excessive depletion of HREE in the two samples from Sites 1227 and 1228 might be a result of excessive garnet precipitation and sequestration at depth. Alternatively, this REE pattern is similar to those of adakites and Archean tonalite, trondhjemite, and granodiorite (TTG) suites present within southern Peru (Condie, 2005; Martin, 1993, 1999) samples.

Ash Layer Correlations

Ash layer correlations between sites were based on lithology, stratigraphic position, and major element geochemistry and were refined through REE geochemistry. Most ash layers from Sites 1228 and 1229 are lithologically similar, with the primary difference being the abundance of volcanic glass or pumice, and half of Site 1229 ash layers correlate with Site 1228 ash layers even upon comparing volcanic glass and pumice abundances (Table **T3**). However, some of these ash layers do not correlate well stratigraphically.

As previously discussed, most Leg 201 ash layers display the same general major element oxide trends between sites for both glass and whole-rock analyses. However, no ash layers correlate perfectly based on major element oxides. Because of the lack of definite correlations of
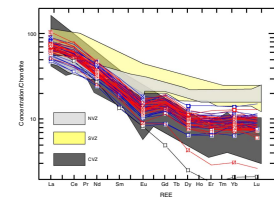
ash layers based on lithology, stratigraphic position, and major element oxide concentrations, REE geochemistry was used to refine possible correlations between Leg 201 sites; these correlations are displayed in Figure F12. This figure shows that three ash layers correlate between Sites 1228 and 1229 and the REE pattern for one ash layer from Site 1228 is similar to that of the one layer at Site 1227 (Fig. F12), in that both display steep REE patterns.

Explosive Volcanic Cycles

Many studies have recorded the explosive volcanic cycles of land eruptions through documentation of ash layers in deep-sea sediments (Prueher and Rea, 2001; Pouclet et al., 1990; Paterne et al., 1990; Ledbetter and Sparks, 1979; Kennett et al., 1977; Donnelly, 1976). The thickness and number of Type 1 ash layers have been summed for each Leg 201 site in this study and have been plotted per half million year time increments (Fig. F13) for the purpose of depicting the explosive volcanic cycles for the Central Andes. One limitation in utilizing Leg 112 sedimentation rate curves to depict ash occurrence per half million years from Leg 201 is that the sedimentation rate curves from Leg 112 only extend to 120 mbsf, whereas Type 1 ash is present in Leg 201 Sites 1228 and 1229 cores to 152.74 and 159.55 mbsf, respectively. Additionally, another limitation is that Leg 112 sedimentation rate curves are constructed based upon the first and last occurrence of either diatoms or nannoplankton, which may yield large time errors (Fig. F13).

This summation does not take into account accumulations, pods, very thin laminae (<1 mm), or diagenetically altered layers and therefore provides minimal estimations at best. Additionally, all Leg 201 sites have been affected by sedimentary hiatuses (Fig. F5), and some sections of core display evidence of possible slump deposits and/or turbidites. These features could be a significant factor in the disappearance of ash layers from the marine record. Prevailing wind direction and marine currents are two limiting factors that should also be taken into account when recording volcanic cycles from ash within deep-sea sediments (Pouclet et al., 1990). Because the closest known volcanic source is >400 km from the study region (Fig. F1), it is apparent that wind direction and, to a smaller extent, ocean current may be responsible for depositing ash far offshore. Figure F3 displays the southwestern trade winds that circulate north-northwestward along the Chile coast. These winds appear to follow the Chilean littoral up to the Peru coast, where their direction takes on a southeasterly path that parallels the Peruvian coast. These winds, coupled with the coriolis effect, cause a deflection in the Humboldt Current, which circulates northward along the South American western coast to the surrounding area of the Equator, thus severing the current from the Peruvian coast (Garcia, 1994). This suggests that volcanic ash erupted into the atmosphere from northern Chile and/or southern Peru would have been transported into the study region by the prevailing trade winds along western South America.

Figure F13 displays ash layer thickness and the number of ash layers per half million year time increments. Explosive eruption cycles for the Andean region have been deduced from these data. Our record of volcanic cycles indicates that explosive activity was less intense during the Miocene, in which one ash layer (1.3 cm) was deposited, compared to that of the Pliocene and Pleistocene, which experienced most of the explosive volcanic activity in which 52 ash layers (total thickness equal to 208.6 cm) and 14 ash layers (total thickness equal to 122.1 cm) were de-

F12. Ash layer correlations and corresponding REE pairs, p. 31.
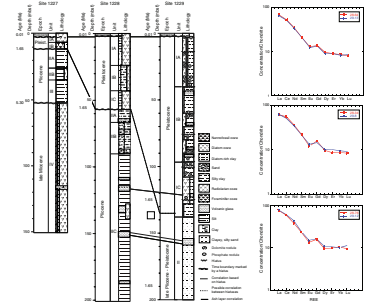
F13. Ash layer thickness and number of ash layers, p. 32.
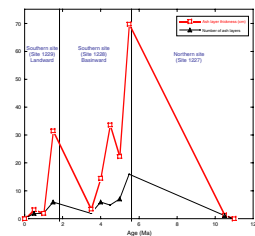
posited, respectively. These data are consistent with the previous study of Pouclet et al. (1990); however, these data indicate that explosive activity during the Pliocene and Pleistocene was more intense than previously reported. Additionally, the total thickness of primary ash within all three Leg 201 sites is equal to 332.0 cm, which is ~24 times as much primary ash reported by Pouclet et al. (1990; 14 cm) within the previously occupied sites of Leg 112. However, Pouclet et al. (1990) report three Miocene volcanic phases for the northern and southern sites of Leg 112. Here only one Miocene ash layer is observed within cores from the northern site (Hole 1227A; Pouclet et al. [1990] Site 684), and no Miocene ash is observed for Leg 201 southern sites. This discrepancy is due to two factors: first, only one Miocene ash layer is present within the northern site studied both here (Hole 1227A) and previously (Site 684); the other two layers reported by Pouclet et al. (1990) were in cores from northern sites that were either not examined during this study or were not reoccupied during Leg 201. Second, the southern sites studied by Pouclet et al. (1990) that contained Miocene ash layers were not reoccupied during Leg 201.

DISCUSSION

Volcanoes of the CVZ of the Central Andes are responsible for producing some of the largest volcanic deposits within the Andean chain (e.g., Lindsay et al., 2001; de Silva and Francis, 1991; Francis and de Silva, 1989; Sparks et al., 1985; Hall and Calle, 1982; Lahesen, 1982; Baker, 1981; Tosdal et al., 1981; Baker and Francis, 1978; Noble et al., 1974). The large ignimbrite deposits of this region are of the most significance for this study because they indicate the likelihood of airborne ash (Baker and Francis, 1978) and large plinian-style eruptions, which can produce widespread air fall ash (Fisher and Schmincke, 1984), such as that deposited off the Peru coast and present in cores from all three Leg 201 sites studied.

From the detailed examination of Leg 201 cores drilled off the coast of Peru, we have documented ash layers in Miocene, Pliocene, Pleistocene, and Holocene sediments that amplify the signal of eruptive activity from the Andes with nearly 25 times more primary ash layers reported than in previous marine ash layer studies. We also note an even greater thickness of diagenetically altered ash deposits that are likely representative of major explosive volcanic events owing to the distance offshore of our study area.

The comparison of Leg 201 ash layers with land and marine studies is based on both whole-rock and glass geochemistry. These comparisons can suggest which volcanic zone(s) of the Andes provide the provenance for the ash layers but cannot determine the individual volcano from which these layers were erupted. We surmise that the majority of the ash layers we analyzed have affinities with compositions from the CVZ and are not likely derived from the NVZ or SVZ.

The explosive cycles of Andean volcanoes are recorded in the marine sediments of all Leg 201 sites studied, as well as within the voluminous deposits of ignimbrites on land. Each of these regions has been studied and documents concurrent cycles of explosive activity. In general, the land records of Baker and Francis (1978) and Francis and Hawkesworth (1994) suggest that the greatest volume of eruptions was experienced during the Miocene (1300 km^3), with a significant decrease in activity during the Pliocene (650 km^3), and even less volcanic ash was deposited

during Pleistocene and Holocene (275 km³) within the northern area of their study regions. Whereas our Type 1 ash record records only a single event in the Miocene with significant ash deposited, there are at least three more layers of diagenetically altered ash in this section. Type 1 ash layers are most common our Pliocene record, and there is a lower number of ash layers and cumulative ash layer thickness in Pleistocene–Holocene sediments. Additionally, three altered ash layers (containing between 15% and 60% biogenic material) are present in Holocene sediments at our the southern sites, indicating the possible occurrence of three large-magnitude eruptions not preserved within the land record for this time period.

ACKNOWLEDGMENTS

REFERENCES

Adams, N.K., de Silva, S.L., Self, S., Salas, G., Schubring, S., Permenter, J.L., and Arbesman, K., 2001. The physical volcanology of the 1600 eruption of Huaynaputina, southern Peru. *Bull. Volcanol.*, 62(8):493–518. doi:10.1007/s004450000105

Baker, M.C.W., 1981. The nature and distribution of upper Cenozoic ignimbrite centers in the Central Andes. *J. Volcanol. Geotherm. Res.*, 11(2–4):293–315. doi:10.1016/0377-0273(81)90028-7

Baker, M.C.W., and Francis, P.W., 1978. Upper Cenozoic volcanism in the Central Andes—ages and volumes. *Earth Planet. Sci. Lett.,* 41(2):175–187. doi:10.1016/0012-821X(78)90008-0

Condie, K.C., 2005. TTGs and adakites: are they both slab melts? *Lithos,* 80, 1:4, 33–44.

D'Hondt, S.L., Jorgensen, B.B., Miller, D.J., et al., 2003. *Proc. ODP, Init. Repts.*, 201 [CD-ROM]. Available from Ocean Drilling Program, Texas A&M University, College Station TX 77845-9547, USA.

D'Orazio, M., Innocenti, F., Manetti, P., Tamponi, M., Tonarini, S., Gonzalez-Ferran, O., Lahsen, A., and Omarini, R., 2003. The Quaternary calc-alkaline volcanism of the Patagonia Andes close to the Chile triple junction: geochemistry and petrogenesis of volcanic rocks from the Cay and Maca volcanoes (~45°S, Chile). *J. South Am. Earth Sci.,* 16(4):219–242. doi:10.1016/S0895-9811(03)00063-4

de Silva, S.L., 1989. Geochronology and stratigraphy of the ignimbrites from the 21°30′ S to 23°30′S portion of the Central Andes of northern Chile. *J. Volcanol. Geotherm. Res.*, 37(2):93–131. doi:10.1016/0377-0273(89)90065-6

de Silva, S.L., and Francis, P.W., 1989. Correlation of large ignimbrites–two case studies from the Central Andes of northern Chile. *J. Volcanol. Geotherm. Res.*, 37(2):133–149. doi:10.1016/0377-0273(89)90066-8

de Silva, S.L., and Francis, P.W., 1991. *Volcanoes of the Central Andes:* New York (Springer-Verlag).

de Silva, S.L., and Zielinski, G.A., 1998. Global influence of the AD 1600 eruption of Huaynaputina, Peru. *Nature (London, U. K.),* 393(2):455–458. doi:10.1038/30948

Donnelly, T.W., 1976. Tertiary explosive volcanic activity in the eastern equatorial Pacific Ocean: Sites 320 and 321, DSDP Leg 34. *In* Yeats, R.S., Hart, S.R., et al., *Init. Repts. DSDP,* 34: Washington (U.S. Govt. Printing Office), 605–609.

Dorendorf, F., Churikova, T., Koloskov, A., and Wörner, G., 2000. Late Pleistocene to Holocene activity at Bakening Volcano and surrounding monogenetic centers (Kamchatka): volcanic geology and geochemical evolution. *J. Volcanol. Geotherm. Res.*, 104(1-4):131–151. doi:10.1016/S0377-0273(00)00203-1

Dostal, J., Dupuy, C., and Lefevre, C., 1977. Rare earth element distribution in Plio-Quarternary volcanic rocks from southern Peru. *Lithos,* 10(3):173–183. doi:10.1016/0024-4937(77)90045-7

Droux, A., and Delaloye, M., 1996. Petrography and geochemistry of Plio-Quaternary calc-alkaline volcanoes of southwestern Columbia. *J. South Am. Earth Sci.,* 9(1-2):27–41. doi:10.1016/0895-9811(96)00025-9

Fisher, R.V., and Schmincke, H.-U., 1984. *Pyroclastic Rocks:* New York (Springer-Verlag).

Francis, P.W., and Baker, M.C.W., 1978. Sources of two large ignimbrites in the Central Andes: Some Landsat evidence. *J. Volcanol. Geotherm. Res.,* 4(1-2):81–87. doi:10.1016/0377-0273(78)90029-X

Francis, P.W., and de Silva, S.L., 1989. Application of the Landsat Thematic Mapper to the identification of potentially active volcanoes in the Central Andes. *Remote Sens. Environ.,* 28:245–255. doi:10.1016/0034-4257(89)90117-X

Francis, P.W., and Hawkesworth, C.J., 1994. Late Cenozoic rates of magmatic activity in the Central Andes and their relationship to continental crust formation and thickening. *J. Geol. Soc., London*, 151:845–854.

Garcia, N.O., 1994. South American climatology. *Quaternary International*, 21:7–27. doi:10.1016/1040-6182(94)90018-3

Gutierrez, F., Gioncada, A., Gonzales Ferran, O., Lahsen, A., and Mazzuoli, R., 2005. The Hudson Volcano and surrounding monogenetic centres (Chilean Patagonia): an example of volcanism associated with ridge-trench collision environment. *J. Volcanol. Geotherm. Res.,* 145(3-4):207–233. doi:10.1016/j.jvolgeores.2005.01.014

Hall, M.L., and Calle, J., 1982. Geochronological control for the main tectonic-magmatic events of Ecuador. *Earth Sci. Rev.,* 18(3-4):215–239. doi:10.1016/0012-8252(82)90038-1

Hanus, V., and Vanek, J., 1978. Morphology of the Andean Wadati-Benioff Zone, andesitic volcanism, and tectonic features of the Nazca plate. *Tectonophysics,* 44(1-4):65–77. doi:10.1016/0040-1951(78)90063-X

Irvine, T.N., and Baragar, W.R.A., 1971. A guide to the chemical classification of the common volcanic rocks. *Can. J. Earth Sci.,* 8:523–548.

Kennett, J.P., McBirney, A.R., and Thunnell, R.C., 1977. Episodes of Cenozoic volcanism in the Circum-Pacific region. *J. Volcanol. Geotherm. Res.,* 2(2):145–163. doi:10.1016/0377-0273(77)90007-5

Lackschewitz, K.S., and Wallrabe-Adams, H.-J., 1997. Composition and origin of volcanic ash zones in late Quaternary sediments from the Reykjanes Ridge: evidence for ash fallout and ice-rafting. *Mar. Geol.,* 136(3-4):209–224. doi:10.1016/S0025-3227(96)00056-4

Lahsen, A., 1982. Upper Cenozoic volcanism and tectonism in the Andes of northern Chile. *Earth Sci. Rev.,* 18(3-4):285–302. doi:10.1016/0012-8252(82)90041-1

Ledbetter, M.T., 1985. Tephrochronology of marine tephra adjacent to Central America. *Geol. Soc. Am. Bull.,* 96(1):77–82. doi:10.1130/0016-7606(1985)96<77:TOMTAT>2.0.CO;2

Ledbetter, M.T., and Sparks, R.S.J., 1979. Duration of large-magnitude explosive eruptions deduced from graded bedding in deep-sea ash layers. *Geology,* 7(5):240–244. doi:10.1130/0091-7613(1979)7<240:DOLEED>2.0.CO;2

Legros, F., 2001. Tephra stratigraphy of Misti Volcano, Peru. *J. South Am. Earth Sci.,* 14(1):15–29. doi:10.1016/S0895-9811(00)00062-6

Le Maitre, R.W., 1976. The chemical variability of some common igneous rocks. *J. Petrol.,* 17:589–637.

Le Maitre, R.W., Bateman, P., Dudek, A., Keller, J., Lameyre, J., Le Bas, M.J., Sabine, P.A., Schmid, R., Sorensen, H., Streckeisen, A., Woolley, A.R., and Zanettin, B., 1989. *A Classification of Igneous Rocks and Glossary of Terms:* Oxford (Blackwell).

Lindsay, J.M., de Silva, S., Trumbull, R., Emmermann, R., Wemmer, K., 2001. La Pacana caldera, N. Chile: a re-evaluation of the stratigraphy and volcanology of one of the world's largest resurgent calderas. *J. Volcanol. Geotherm. Res.,* 106(1-2):145–173. doi:10.1016/S0377-0273(00)00270-5

Martin, H., 1993. The mechanisms of petrogenesis of the Archaean continental crust—comparison with modern processes. *Lithos,* 30(3-4):373–388. doi:10.1016/0024-4937(93)90046-F

Martin, H., 1999. Adakitic magmas: modern analogues of Archaen graintoids. *Lithos,* 46(3):411–429. doi:10.1016/S0024-4937(98)00076-0

Matteini, M., Mazzuoli, R., Omarini, R., Cas, R., and Maas, R., 2002. The geochemical variations of the upper Cenozoic volcanism along the Calama-Olacapato-El Toro transversal fault system in central Andes (~24°S): petrogenetic and geodynamic implications. *Tectonophysics,* 345(1-4):211–227. doi:10.1016/S0040-1951(01)00214-1

Monzier, M., Robin, C., Samaniego, P., Hall, M.L., Cotton, J., Mothes, P., and Arnaud, N., 1999. Sangay volcano, Ecuador: structural development, present activity and petrology. *J. Volcanol. Geotherm. Res,* 90(1-2):49–79. doi:10.1016/S0377-0273(99)00021-9

Noble, D.C., McKee, E.H., Farrar, E., and Petersen, U., 1974. Episodic Cenozoic volcanism and tectonism in the Andes of Peru. *Earth Planet. Sci. Lett.,* 21:213–220.

Paterne, M., Labreyrie, J., Guichard, F., Mazaud, A., and Maitre, F., 1990. Fluctuations of the Campanian explosive volcanic activity (South Italy) during the past 190,000 years, as determined by marine tephrochronology. *Earth Planet. Sci. Lett.,* 98(2):166–174. doi:10.1016/0012-821X(90)90057-5

Pattan, J.N., Shane, P., and Banakar, V.K., 1999. New occurrence of youngest Toba Tuff in abyssal sediments of the Central Indian Basin. *Mar. Geol.*, 155(3-4):243–248. **doi:10.1016/S0025-3227(98)00160-1**

Petrinovic I.A., Riller, U., and Brod, J.A., 2005. The Negra Muerta Volcanic Complex, southern Central Andes: geochemical characteristics and magmatic evolution of an episodically active volcanic centre. *J. Volcanol. Geotherm. Res.,* 140(4):295–320. **doi:10.1016/j.jvolgeores.2004.09.002**

Pouclet, A., Cambray, H., Cadet, J.-P., Bourgois, J., and De Wever, P., 1990. Volcanic ash from Leg 112 off Peru. *In* Suess, E., von Huene, R., et al., *Proc. ODP, Sci. Results,* 112: College Station, TX (Ocean Drilling Program), 465–480.

Prueher, L.M., and Rea, D.K., 2001. Tephrochronology of the Kamchatka-Kurile and Aleutian arcs: evidence for volcanic episodicity. *J. Volcanol. Geotherm. Res.*, 106(1-2):67–84. **doi:10.1016/S0377-0273(00)00266-3**

Richards, J.P., and Villeneuve, M., 2001. The Llullaillaco Volcano, northwest Argentine: construction by Pleistocene volcanism and destruction by sector collapse. *J. Volcanol. Geotherm. Res.*, 105(1-2):77–105. **doi:10.1016/S0377-0273(00)00245-6**

Rickwood, P.C., 1989. Boundary lines within petrological diagrams which use oxides of major and minor elements. *Lithos,* 22(4):247–263. **doi:10.1016/0024-4937(89)90028-5**

Rollinson, H.R., 1993. *Using Geochemical Data, evaluation, Presentation, Interpretation:* London (Pearson/Prentice Hall).

Shane, P., 2000. Tephrochronology: a New Zealand case study. *Earth Sci. Rev.,* 49(1-4):223–259. **doi:10.1016/S0012-8252(99)00058-6**

Shipboard Scientific Party, 2003. Leg 201 summary. In D'Hondt, Jørgensen, B.B., Miller, D.J., et al., *Proc. ODP, Init. Repts.,* 201: College Station TX (Ocean Drilling Program), 1–81. [**HTML**]

Siebel, W., Schnurr, W.B.W., Hahne, K., Kraemer, B., Trumbull, R.B., van den Bogaard, P., and Emmermann, R., 2001. Geochemistry and isotope systematics of small- to medium-volume Neogene-Quaternary ignimbrites in the southern central Andes: evidence for derivation from andesitic magma source. *Chem. Geol.,* 171(3-4):213–237. **doi:10.1016/S0009-2541(00)00249-7**

Sparks, R.S.J., Francis, P.W., Hamer, R.D., Pankhurst, R.J., O'Callaghan, L.O., Thorpe, R.S., and Page, R., 1985. Ignimbrites of the Cerro Galan Caldera, NW Argentina. *J. Volcanol. Geotherm. Res.*, 24(3-4):205–248. **doi:10.1016/0377-0273(85)90071-X**

Suess, E., von Huene, R., et al., 1990. *Proc. ODP, Sci. Results,* 112: College Station, TX (Ocean Drilling Program).

Thorpe, R.S., and Francis, P.W., 1979. Variations in Andean andesite compositions and their petrogenetic significance. *Tectonophysic*s, 57(1):53–70. **doi:10.1016/0040-1951(79)90101-X**

Thouret, J.C., Davila, J., Rivera, M., Gourgaud, A., Eissen, J.P., Pennec, J.L.L., and Juvigne, E., 1997. The largest explosive eruption (VEI 6) in historical times (1600 AD) in the Central Andes at Huaynaputina, Southern Peru. *Earth Planet. Sci. Lett.,* 325:931–938.

Thouret, J.C., Juvigne, E., Gourgaud, A., Boivin, P., and Davila, J., 2002. Reconstruction of the AD 1600 Huaynaputina eruption based on the correlation of geologic evidence with early Spanish chronicles. *J. Volcanol. Geotherm. Res.*, 115(3-4):529–570. **doi:10.1016/S0377-0273(01)00323-7**

Tosdal, R.M., Farrar, E., and Clark, A.H., 1981. K-Ar geochronology of the late Cenozoic volcanic rocks of the Cordillera Occidental, southernmost Peru. *J. Volcanol. Geotherm. Res.*, 10(1-3):157–173. **doi:10.1016/0377-0273(81)90060-3**

Trumbull, R.B., Wittenbrink, R., Hahne, K., Emmermann, R., Büsch, W., Gerstenberger, H., and Siebel, W., 1999. Evidence for Late Miocene to Recent contamination of arc andesites by crustal melts in the Chilean Andes (25°–26°S) and its geodynamic implications. *J. South Am. Earth Sci.,* 12(2):135–155. **doi:10.1016/S0895-9811(99)00011-5**

Vatin-Perignon, N., Oliver, R.A., Goemans, P., Keller, F., Briqueu, L., and Salas, G.A., 1992. Geodynamic interpretations of plate subduction in the northernmost part of the Central Volcanic Zone from the geochemical evolution and quantification of the crustal contamination of the Nevado Solimana volcano, southern Peru. *Tectonophysics,* 205(1-3):329–355. doi:10.1016/0040-1951(92)90434-8

Vatin-Perignon, N., Poupeau, G., Oliver, R.A., La Venu, A., Labrin, F., Keller, F., and Bellot-Gurlet, L., 1996. Trace and rare-earth element characteristics of acidic tuffs from Southern Peru and Northern Bolivia and a fission-track age for the Sillar of Arequipa. *J. South Am. Earth Sci.,* 9(1-2):91–109. doi:10.1016/0895-9811(96)00030-2

Yeats, R.S., Hart, S.R., et al., 1976. *Init. Repts DSDP,* 34: Washington (U.S. Govt. Printing Office).

Figure F1. The Central Volcanic Zone (CVZ; lighter shaded region) of the Andes, the location of land studies (black shaded regions), and the inset (magnified to the left) displays ODP Legs 201 and 112 and DSDP Leg 34 site locations. The black triangle within the CVZ of the inset is the location of the northernmost volcano within the CVZ (de Silva and Francis, 1991). Modified from D'Hondt, Jørgensen, Miller, et al., (2003).
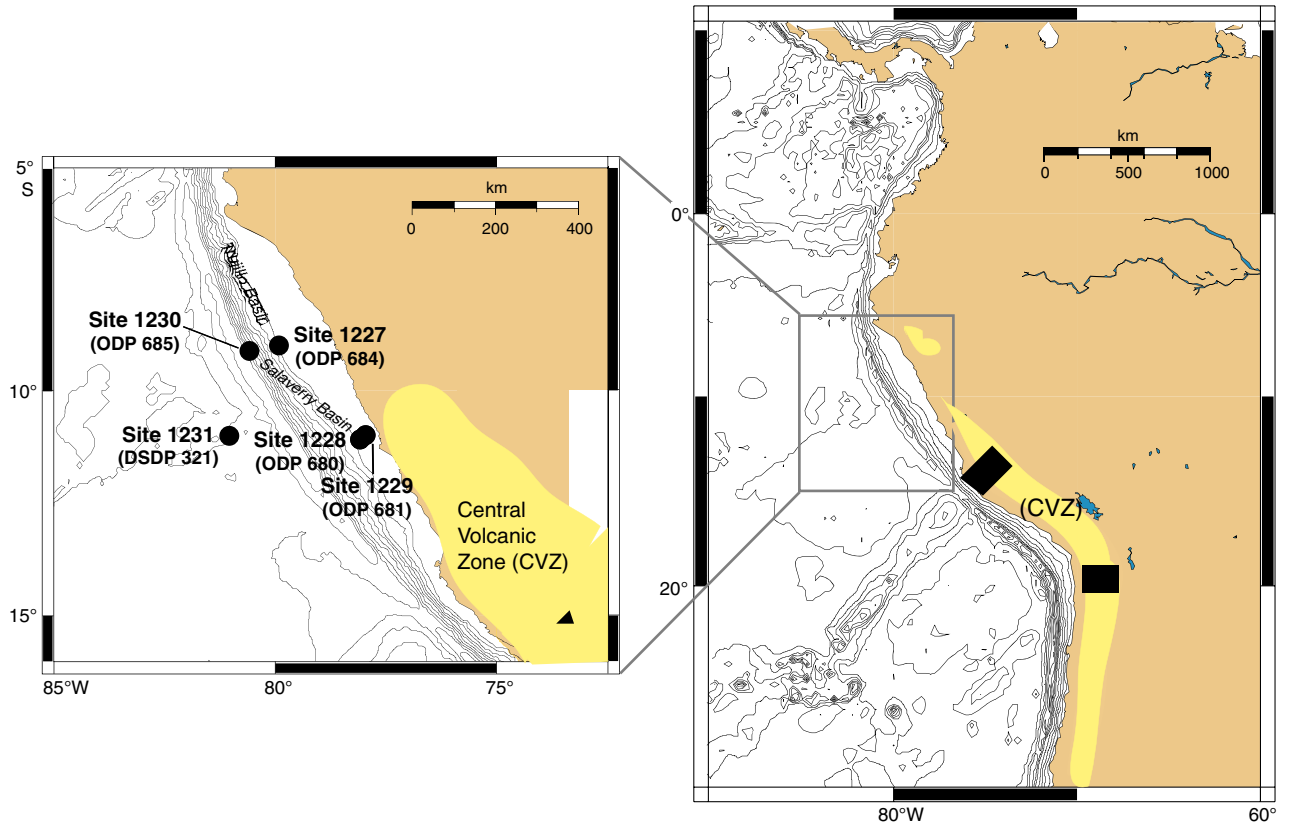
Figure F2. A. The volcanic zones of the Andes (northern volcanic zone [NVZ], central volcanic zone [CVZ], and southern volcanic zone [SVZ]) are located along the western margin of South America. **B.** The areal exposure of Cenozoic–Holocene volcanics. Base map is courtesy of National Aeronautics and Space Administration Jet Propulsion Laboratory/Caltech.
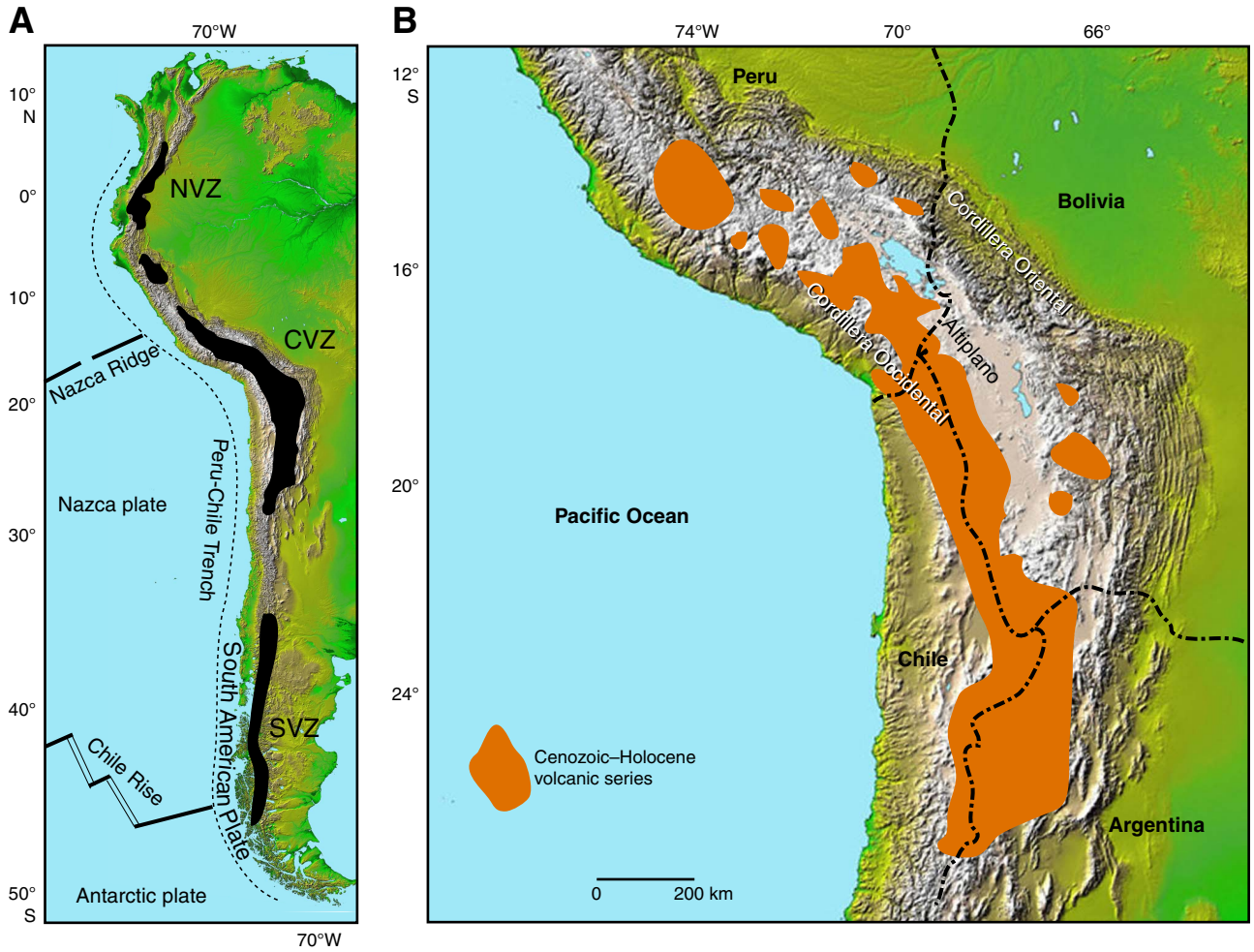
Figure F3. The flow paths of major ocean currents surrounding South America are shown in red and major wind currents are shown in blue. This map is modified from Garcia (1994). Base map courtesy of National Aeronautics and Space Administration Jet Propulsion Laboratory/Caltech.
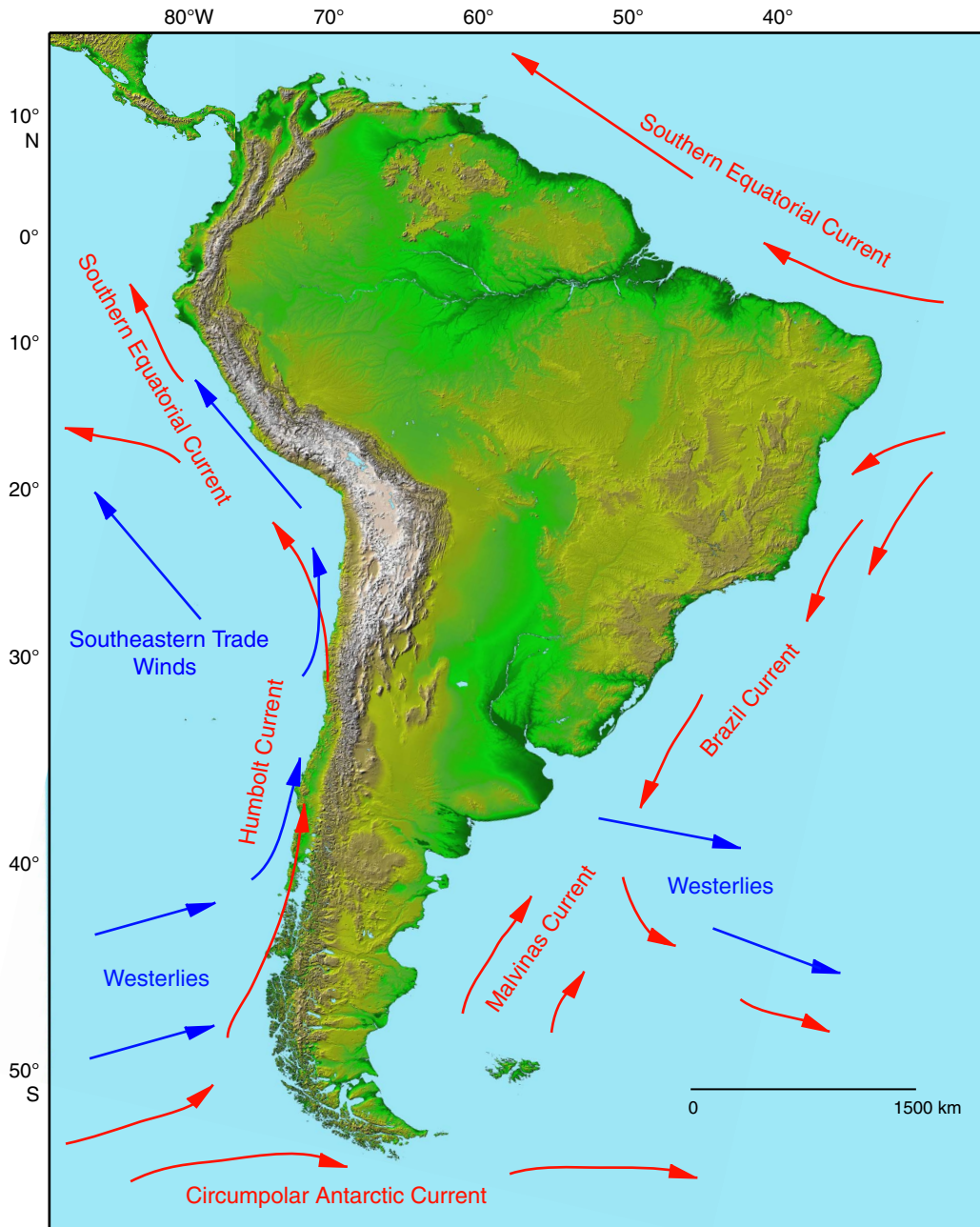
Figure F4. Representative Type 1 ash. Core photograph (left), smear slide (middle), and backscatter electron (right) (BSE) images of three representative ash occurrences for Leg 201 cores. Black arrows point to top and bottom ash layer contacts. From top to bottom, interval 201-1227A-13H-2, 146–147.3 cm, represents ash consisting of ~80% volcanic glass in the form of shards (GS), bubble wall shards (BWS), and vesicular glass (VG); interval 201-1228A-9H-1, 97–101.7 cm, represents ash consisting of vesicular glass (VG), as well as a large glassy aggregate (GA), which consist of various types of glass morphologies; and interval 201-1229A-14H-5, 50–55.6 cm, represents ash consisting of ≥15% pumice (PM), as well as ≥5% volcanic glass.

Interval 201-1227A-13H2, 146-147.3 cm

Interval 201-1228A-9H1, 97-101.7 cm

Interval 201-1229A-14H-5, 50-55.6 cm
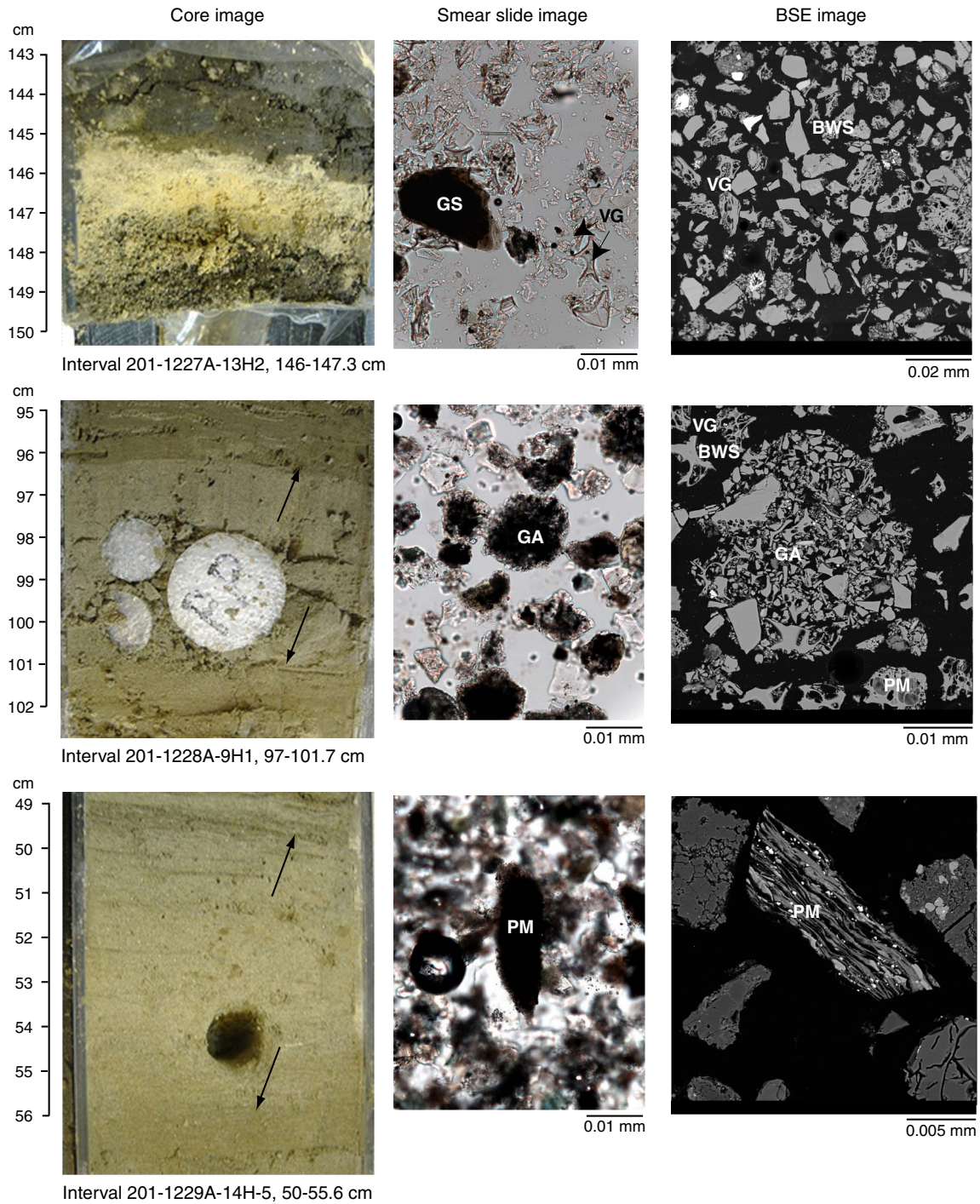
Figure F5. Stratigraphic sections for all three sites. Lightweight tie lines are correlations between hiatuses (dashed line is possible correlation between hiatuses). Heavyweight tie lines are potential correlations between ash layers.
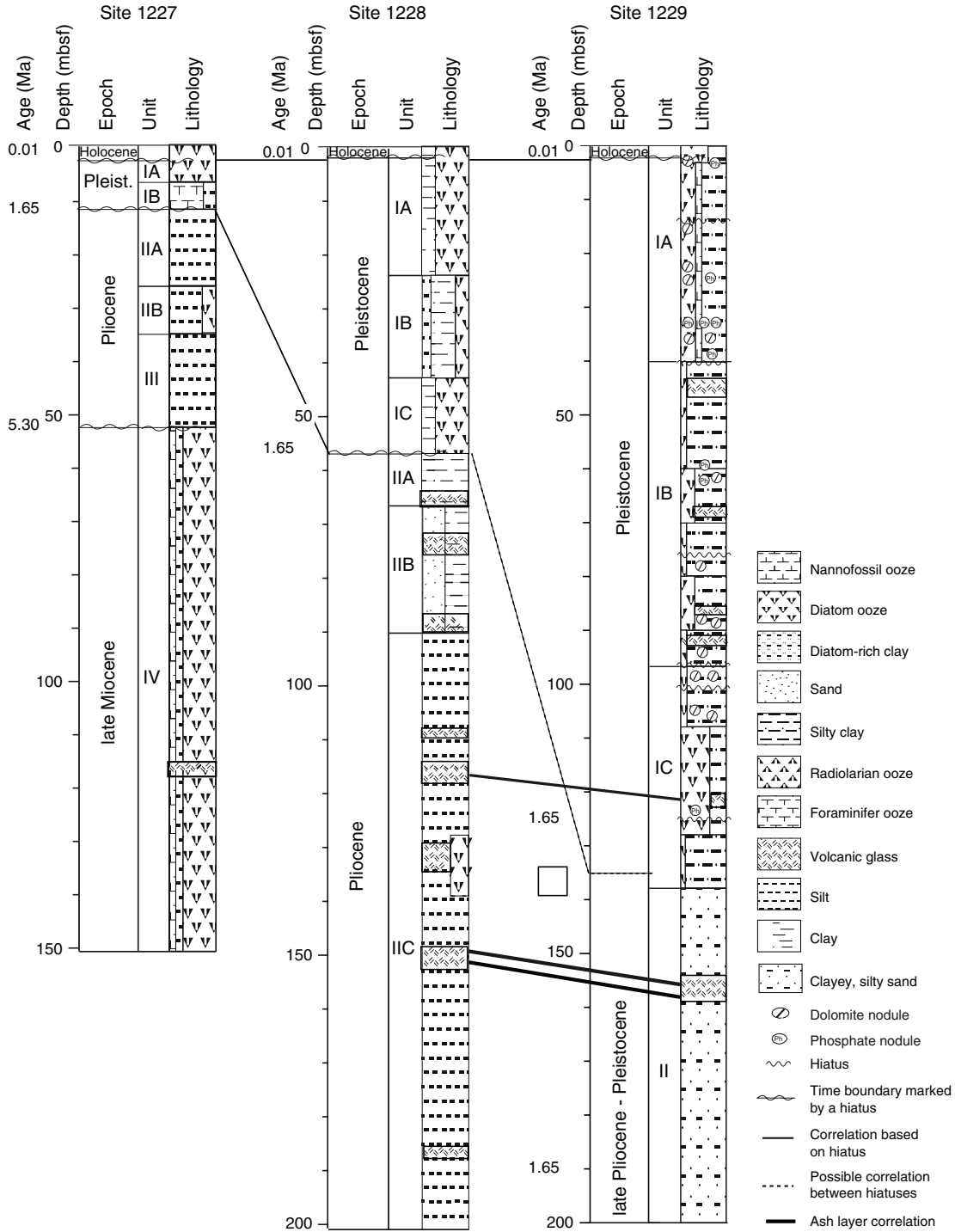
Figure F6. (A) Total alkalis (TAS) vs. silica and (B) potassium vs. silica covariation diagrams for Leg 201 glass analysis. The TAS plot displays the Irvine and Baranger (1971) alkaline/subalkaline (tholeiitic) division line (dashed line). TAS diagram values and nomenclature are from Le Maitre et al. (1989) in Rollinson (1993). B is the subdivision of the subalkaline field (divisions are from the compilation of Rickwood [1989] in Rollinson [1993]). Nomenclature in parentheses is that of Rickwood (1989) and the nomenclature not in parentheses is that of Le Maitre et al. (1989).
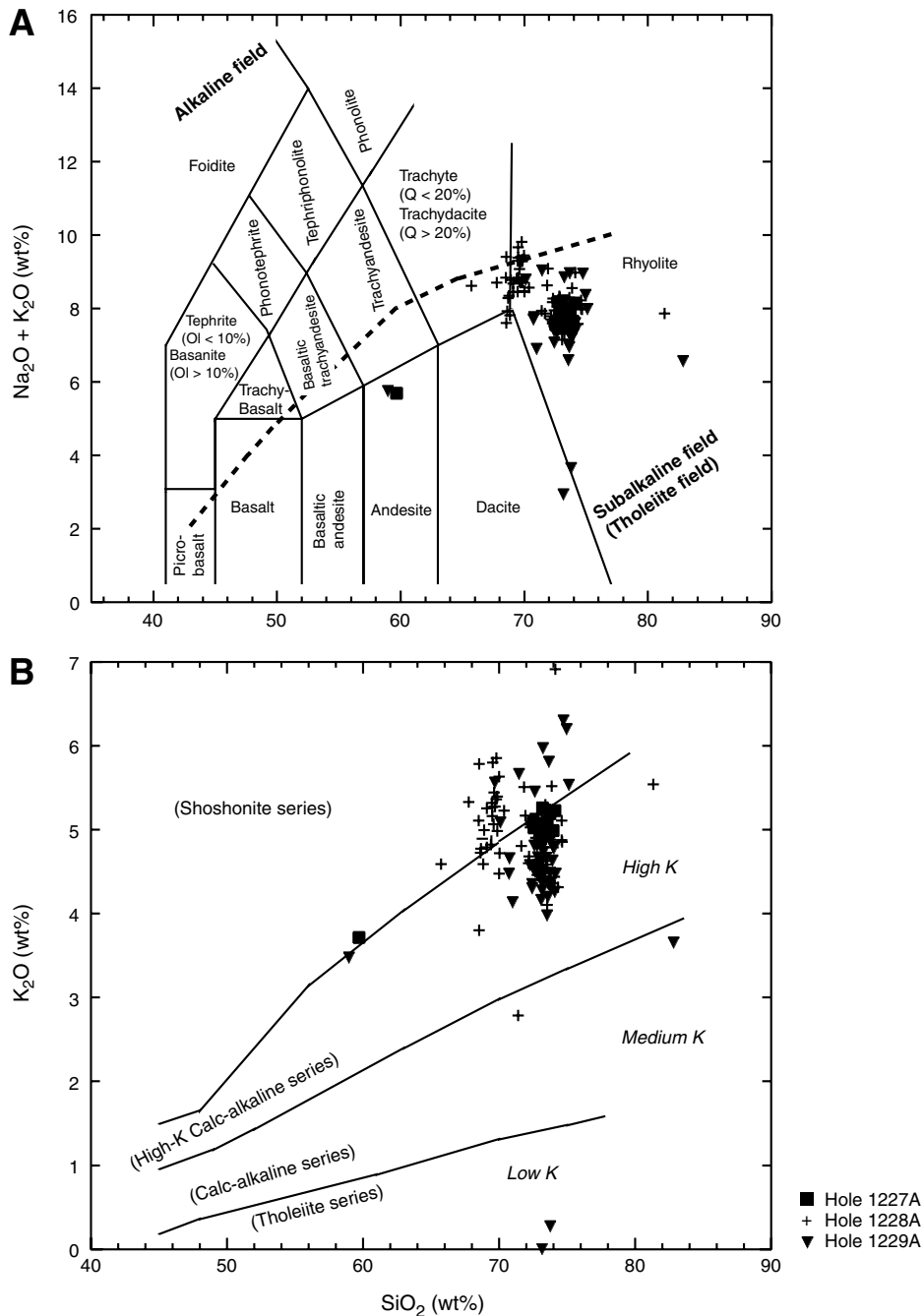
Figure F7. (A) TAS and (B) potassium vs. silica covariation diagrams for average glass values. The TAS diagram shows only the subdivisions for rhyolite and dacite since all values plot within the rhyolitic field. Red ellipses encloses geochemical Group 1 samples, blue ellipses encloses geochemical Group 2 samples.
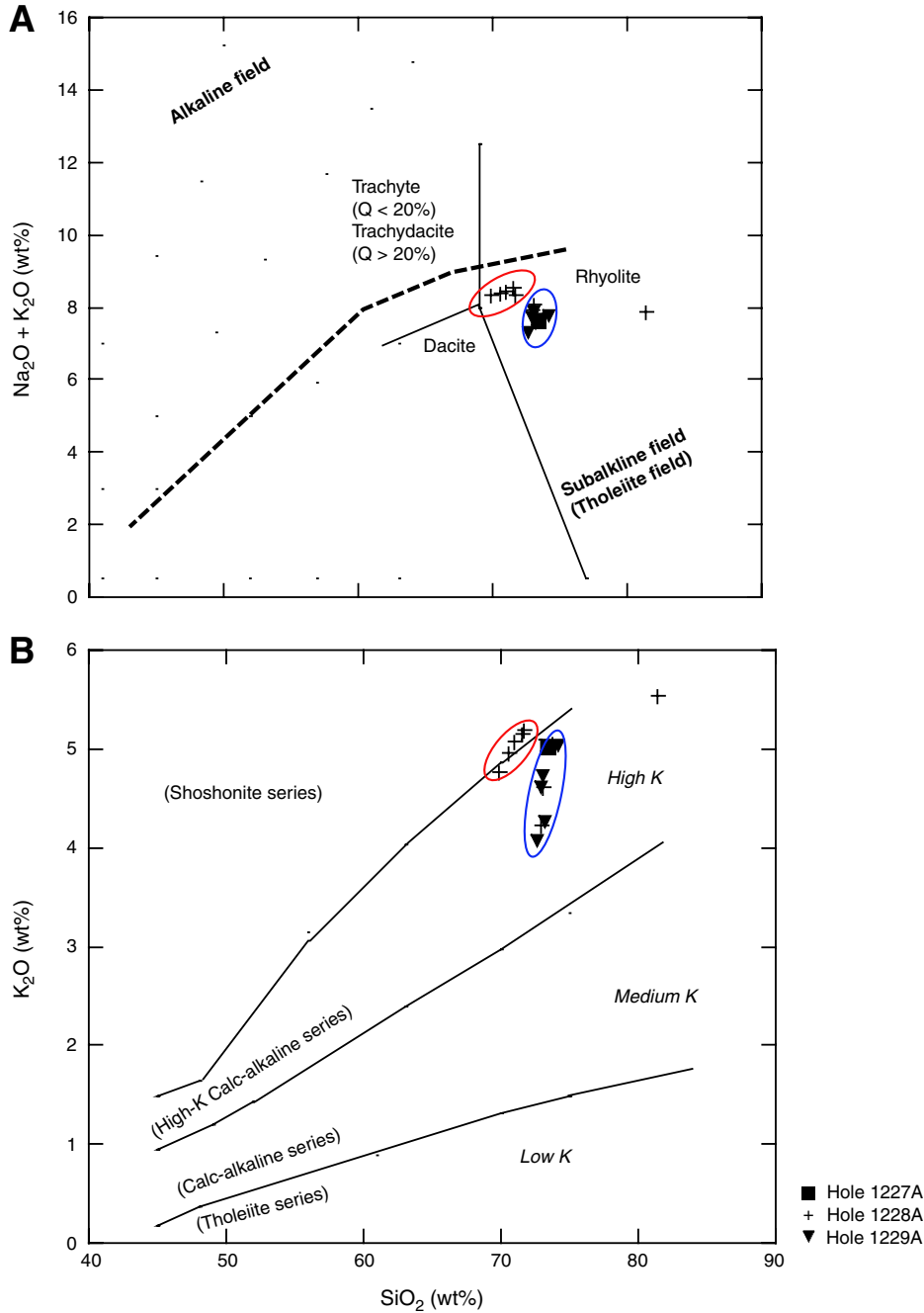
Figure F8. Covariation diagrams for a select group of major element oxides from glass analysis (Leg 201 data are from this study). Representative regions are (1) green (solid line) = CVZ (data from de Silva and Francis, 1989; Legros, 2001; Thorpe and Francis, 1979; Matteini et al., 2002; Sparks et al., 1985; Lindsay et al., 2001; Tosdal et al., 1981; de Silva and Zielinski, 1998; Thouret et al., 2002; Vatin-Perignon et al., 1992; Siebel et al., 2001), (2) maroon (dashed line) = Leg 112 (data from Pouclet et al., 1990), and (3) black (stippled line) = offshore Central America (data from Ledbetter, 1985). No data for regions are available for P_2O_5; it is plotted here for comparison with whole-rock P_2O_5 concentrations.
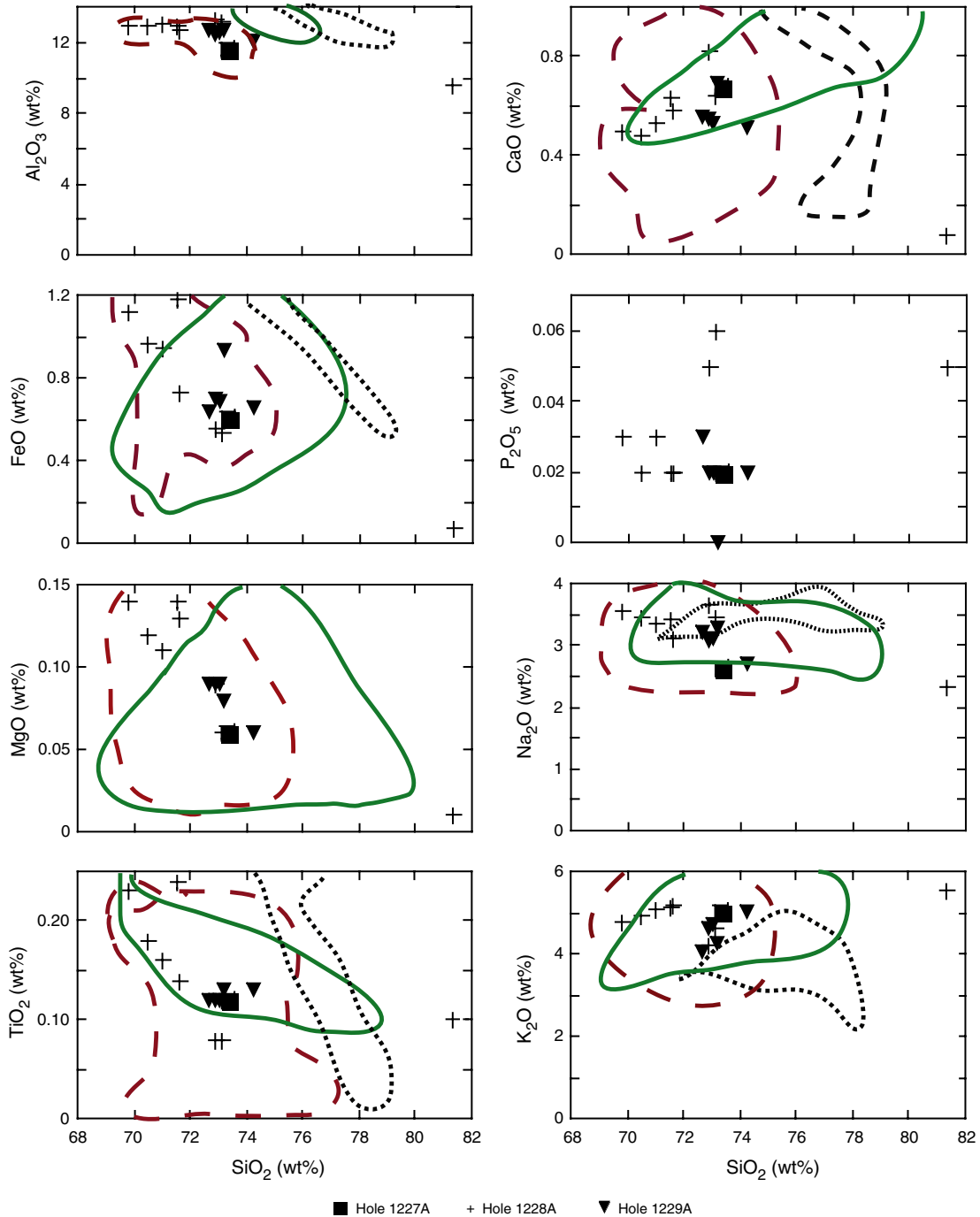
Figure F9. (**A**) TAS covariation diagrams and (**B**) potassium vs. silica for Leg 201 whole-rock analyses. The TAS plot displays the Irvine and Baranger (1971) alkaline/subalkaline (tholeiitic) division line (dashed line). Nomenclature and subdivisions as in Figure F6, p. 25.
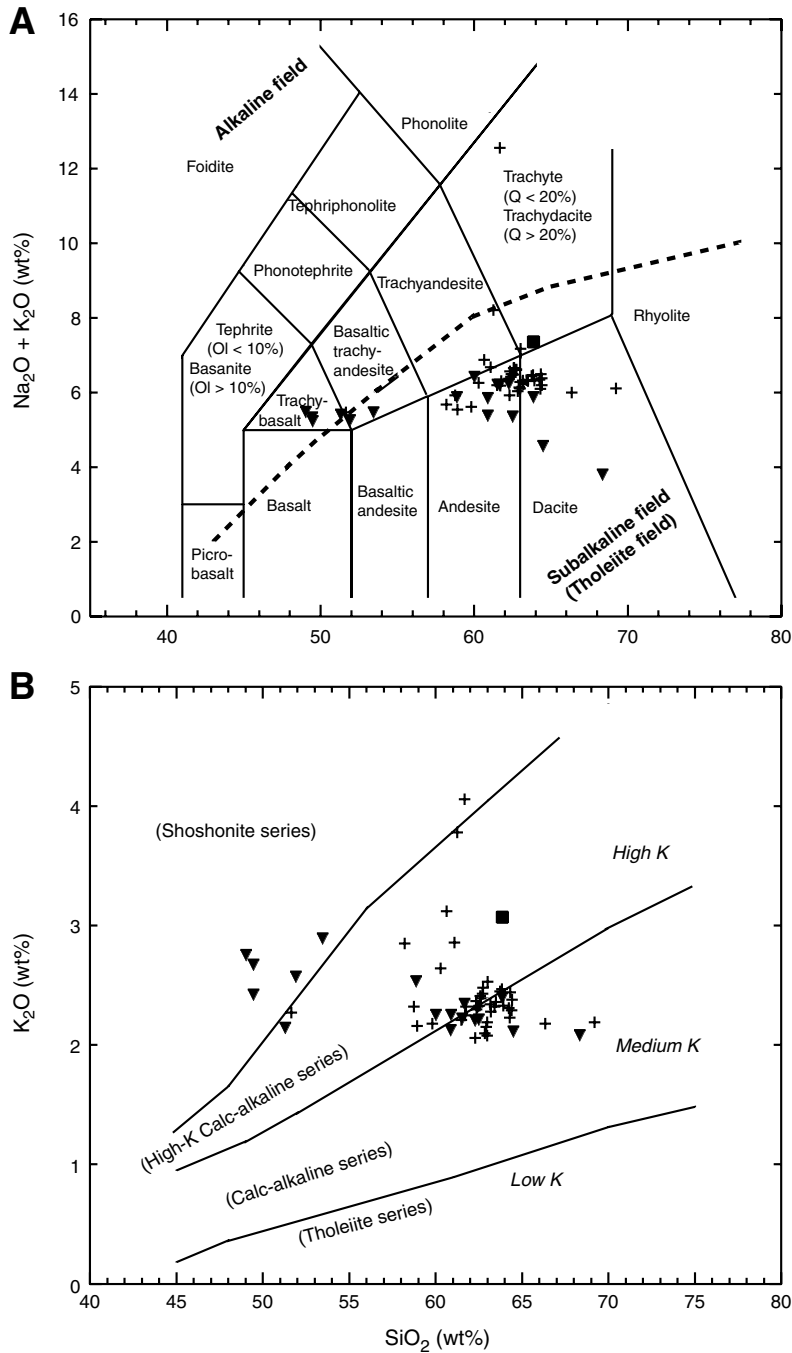
Figure F10. Covariation diagrams for a select group of major element oxides from whole-rock (WR) analysis (WR data are from this study). Representative regions are (1) blue (dashed line) = NVZ (data from Droux and Delaloye, 1996; Monzier et al., 1999), (2) green (solid line) = CVZ (data from same sources as Figure F8, p. 27), and (3) red (stippled line) = SVZ (data from Gutierrez et al., 2005; Trumbull et al., 1999).
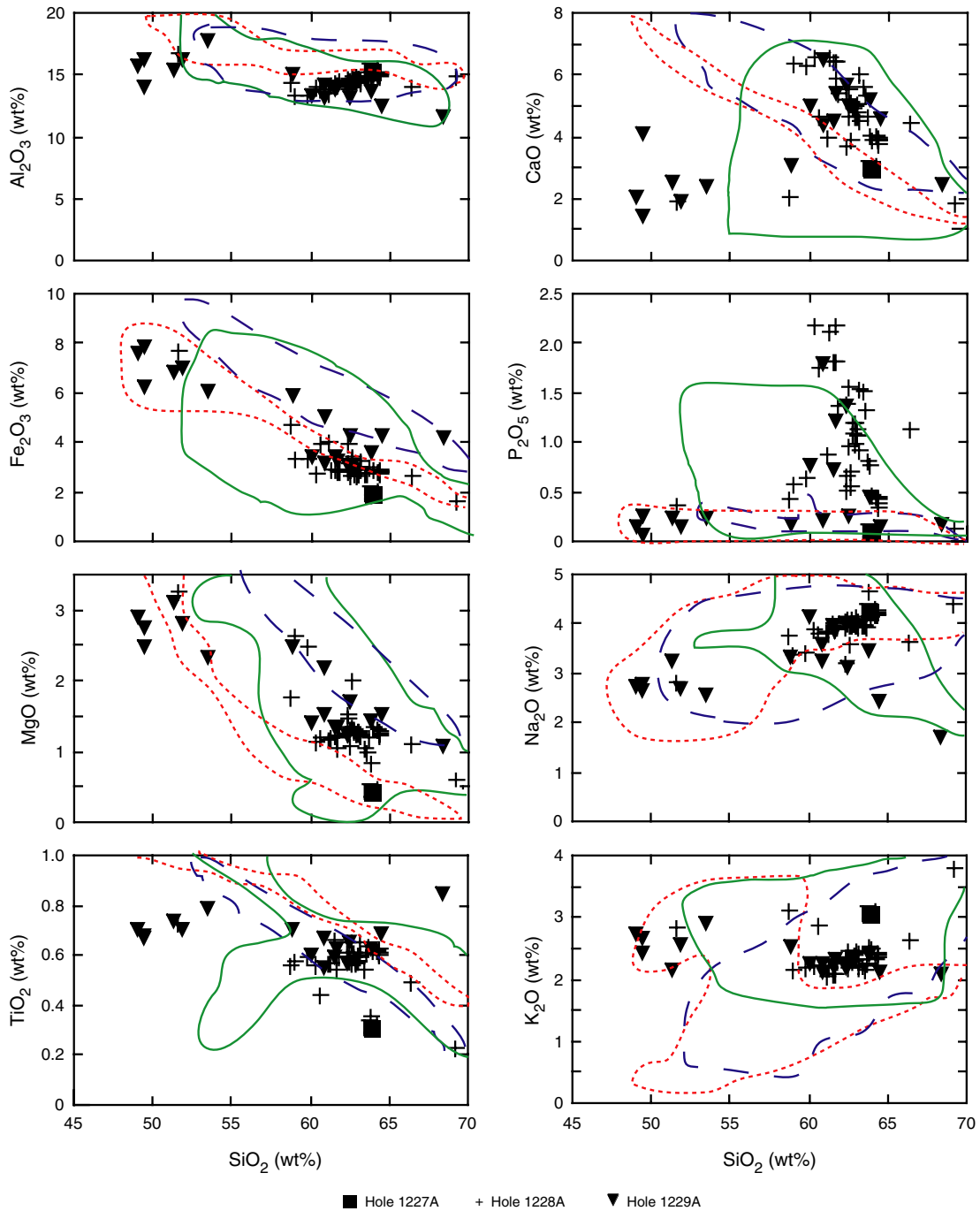
Figure F11. REE data for Leg 201 and the volcanic zones of the Andes. The southern volcanic zone (SVZ) was compiled from Gutierrez et al. (2005) and D'Orazio et al. (2003), the northern volcanic zone (NVZ) is from Droux and Delaloye (1996), and the central volcanic zone (CVZ) is compiled from Petrinovic et al. (2005), Matteini et al. (2002), Richards and Villeneuve (2001), Siebel et al. (2001), Vatin-Perignon et al. (1996), and Dostal et al. (1977). Red, blue, and black lines are rare earth element (REE) plots for Leg 201 ash layers (black = Site 1227, red = Site 1228, blue = Site 1229).
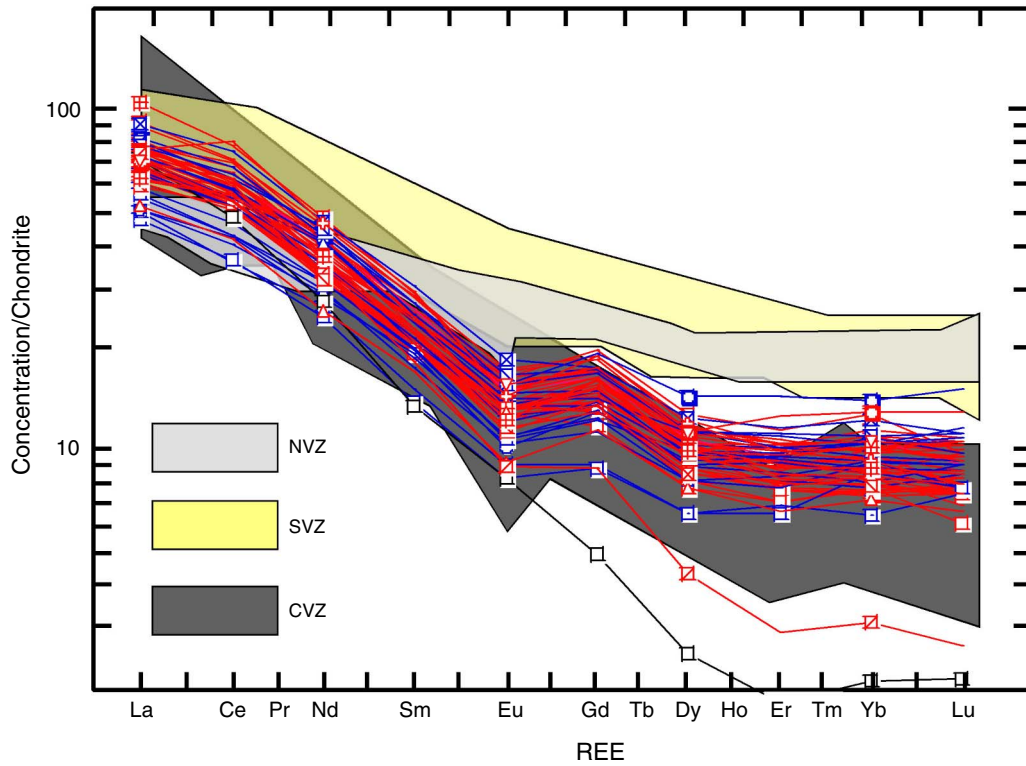
Figure F12. Stratigraphic section displaying ash layer correlations (heavy lines) and corresponding rare earth element (REE) pairs (right panels) for each correlation.
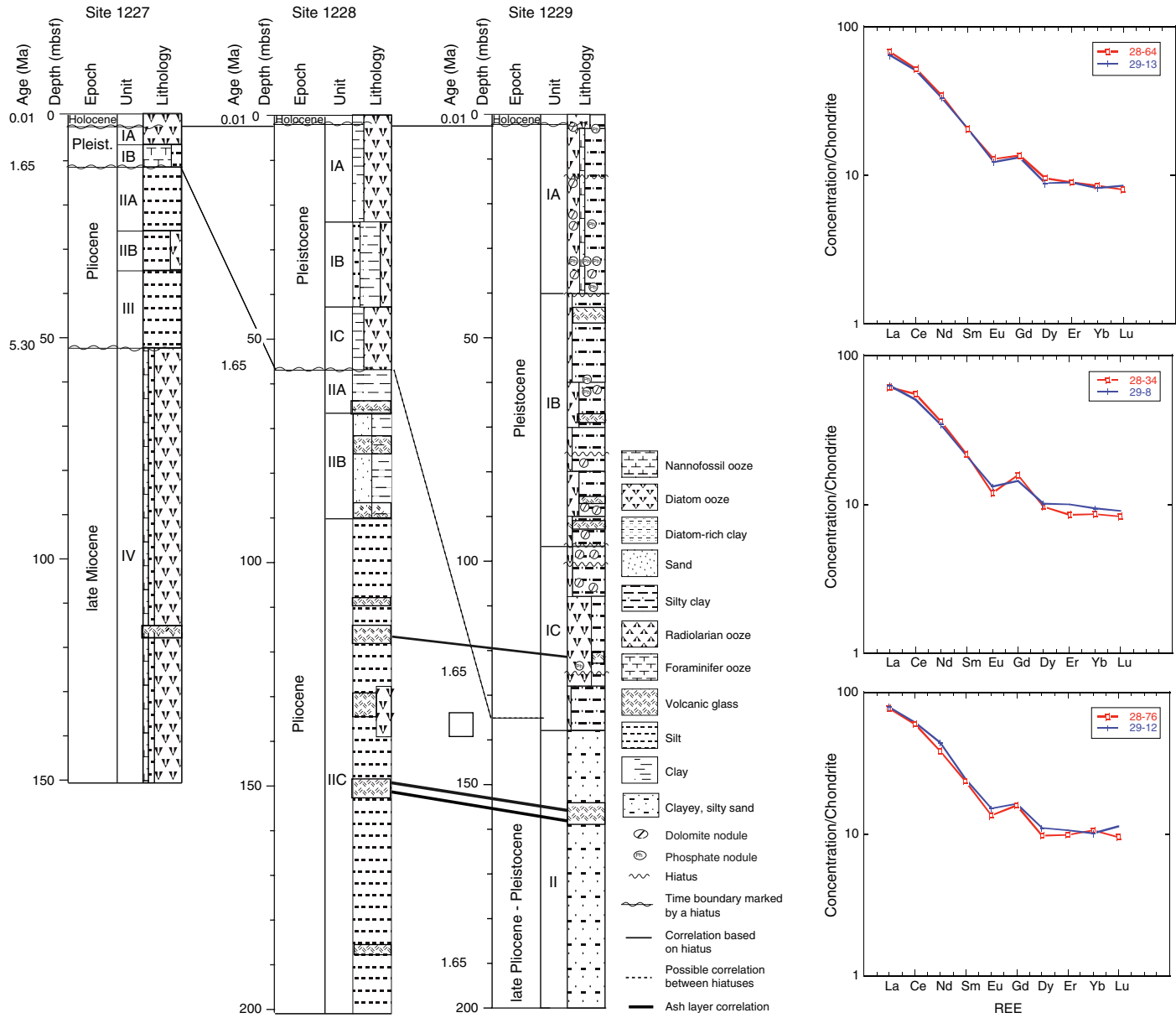
Figure F13. Leg 201 ash layer thickness and number of ash layers plotted per half million year time periods.
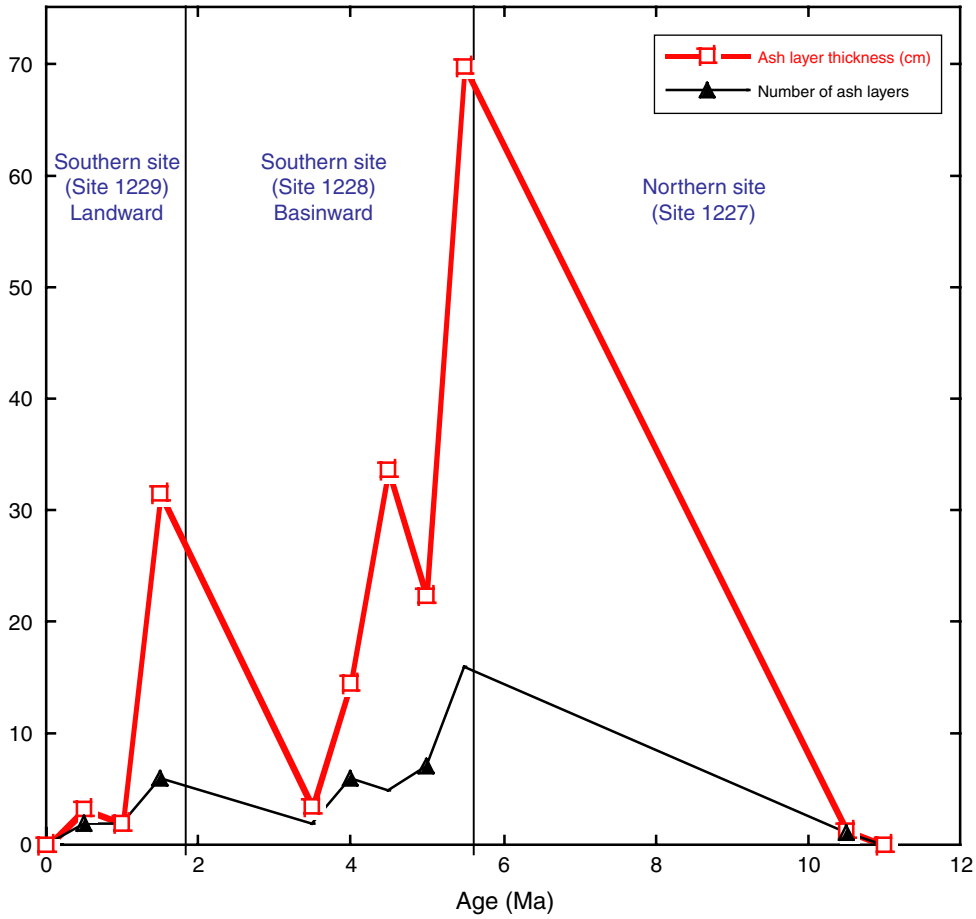
Table T1. Comparison of core recovery between Leg 201 operations and previous occupation (Leg 112).

Leg, site	APC depth (mbsf)	Recovery below previous APC depth (%)
112-684	70	<3
201-1227	150.51	67
112-680	92	4
201-1228	200.9	68
112-681	111	22
201-1229	194.4	44

Table T2. Leg 201 volcanic ash locations reported in Shipboard Scientific Party (2003).

Core, section, interval (cm)	Depth (mbsf)	Notes
201-1227A-		
From lithostratigraphic description:		
7H-1		Not specifically stated: throughout Unit IV (7H-1 to 18CC)
From core description:		
3H-1, 116–118	16–26	Reworked volcanic glass layer
10H	81.6–91.1	Few volcanic accumulations
11H	91.1–100.6	Orange spots with plagioclase-bearing volcanic glass
12H	100.6–110.1	Rich in volcanic glass
13H-3	110.0–119.6	3-cm-thick gray volcanic ash layer: yellow specks, volcanic glass
From smear slides:		
3H-1, 116	16.26	Plagioclase and silt-bearing volcanic ash (69% volcanic glass)
6H-3, 135	47.95	Clay-bearing volcanic glass–rich carbonate ooze (30% volcanic glass)
14H-2, 70	121.8	Plagioclase-bearing volcanic ash (94% volcanic glass)
201-1228A-		
From lithostratigraphic description:		
1H-1	Uppermost 3 m	Few centimeter thick light gray volcanic ash layers
1H-2	Uppermost 3 m	Few centimeter thick light gray volcanic ash layers
3H	Above 5 m	Three ash layers, within cores 1H and 3H, varying in thickness from 4 and 6 cm, show graded bedding and sharp basal contacts, indicating redistribution of terrigenous and volcanic material on the seafloor
4H-6		Three volcanic ash layers observed
6H-4, 60		Parallel and cross laminations
6H-6, 60		Parallel and cross laminations
From core description:		
1H-1, 99	0.99	
1H-2, 8	1.51	Light gray clay-silt rich layers (presumably of volcanic origin)
2H	4.9–14.4	Pale gray ash, layers containing few isotropic clasts, clay is abundant
3H	14.4–23.9	Three blue and gray volcanic ash layers (4 and 6 cm thick)
3H-7		One ash layer shows graded bedding and erosional base
4H-6	31.4	Contains Three volcanic ash layers
6H	42.9–52.4	Pale blue gray ash layer: diatom-bearing clay-rich volcanic ash
10H		Orange spots rich in volcanic glass (disturbed cores)
From smear slides:		
11H-2	91.4–93	Several sandy layers
1H-1, 99	0.99	Diatom-bearing volcanic glass rich silt
1H-2, 132	2.73	Glauconite-bearing quartz-rich lithic silty sand
6H-4, 70	48.1	Diatom-bearing pyrite and clay-rich diatom ooze (70% volcanic glass)
6H-6, 62	51.02	Diatom and volcanic glass-bearing dolomite (5% volcanic glass)
10H-3, 29	84.1	Quartz and plagioclase and diatom-bearing volcanic glass (84% volcanic glass)
201-1229A-		
From core description:		
5H	33.4–39.9	Gray layers are rich in quartz and contain feldspar and glass
11H	88.9–98.4	Few volcaniclastics throughout core
From smear slides:		
5H-4, 66	38.56	Diatom-bearing volcanic glass-feldspar-quartz rich clay (20% volcanic glass)
11H-3, 13	92.03	Volcanic glass bearing quartz-feldspar and silt-rich clay (5% volcanic glass)
11H-5, 73	95.63	Plagioclase-quartz rich volcanic glass (68% volcanic glass)

Table T3. Leg 201 ash layer description. (**See table notes.** Continued on next page.)

Core, section, interval (cm)	Layer thickness (cm)	Depth (mbsf)	Biogenic	Glass – Pumice + 1	Roundness (Qz)	Description, structure, and contact
Miocene						
201-1227A-						
13H-2, 146–147.6*	1.3	115.07	NA	(98–99)–NA	NA	Buff silt to very fine sand, top gradational, bottom may be erosional
Pliocene						
201-1228A-						
8H-2, 83.5–84	0.5	64.24	1	1–3	1–2	Light gray fine silt-clay, 3%–5% dolomite, thins in center, poorly sorted, top gradational; bottom broken
8H-3, 114–117*	3.0	66.04	1–2	1–30		Light silt, ~5% dolomite, clay pod in base, moderate-well sorted, top: right convex
9H-1, 69.8–72*	2.2	72.09	1	50–NA	NA	Cream clay, ~45% groundmass, few dark coarse crystals, convex to left contacts, one flaser mark
9H-1, 72–73	1.0	72.12	≤1	(0.5–2)–75	1–2	Brown silt, ~1% dolomite, pumice: round, bottom: gradational, both slightly wavy
9H-1, 74.5–77*	2.5	72.15	1–2	1.5–5	1–2	Light gray silt, ~4% dolomite, ~20% coated grains, top: gradational wavy, bottom: slightly inclined
9H-1, 81.5–83	1.5	72.22	1–3	1.5–20	3–5	Brown silt (angular), ~3%–5% round pumice, top: sharp to gradational, bottom: gradational-inclined
9H-1, 97–101.6*	4.6	72.37	NA	(1–2)–(3–5)	NA	Gray-tan silt, ~80% glass-coated grains + 2, normally graded, top gradational
9H-1, 121.4–124*	2.6	72.61	1	1.5–(15–30)		Gray-tan silt, ~5% round pumice, ~2%–3% dolomite, normal grading, ≤60% pumice and ~15% dolomite in bottom half
11H-2, 32.5–37.5*	25.5	91.73	NA	1–(30–40)	<0.5	Gray-tan-black coarse silt-sand, ~1%–2% round pumice, thins to right, ~1.8 cm, bottom: slightly inclined
11H-2, 50.2–52.3*	2.1	91.90	NA	80–(3–5)	1–2	Black-brown clay, ~3%–5% round pumice, finely laminated, top: convex, bottom: slight incline, both gradational
11H-2, 52.3–55	2.7	91.93	NA	75–(1–3)	1–2	Tan-cream fine silt, ~2% round pumice and 55% groundmass, finely laminated, gradational-slightly inclined
11H-2, 55–56.6*	1.6	91.95	1–3	30–10	1	Gray-brown-gray silt with ~20% groundmass, normal grading, slightly inclined, top: gradational
11H-2, 59–60.6*	1.6	91.99	<1	70–10	NA	Cream silt, poor–moderately sorted, sharp top: slight ripple, bottom: planar (possible correlation with Section 201-1227A-13H-2)
14H-2, 8.1–11.7*	3.6	111.98	3	(1–2)–(20–30)	<1–1	Tan-brown-gray coarse silt; distinctly more coarse than layers above and below
14H-2, 116.5–117.5†	1.0	113.06	10	<1–20	1	Gray-tan-brown silt to sand, ~1% round pumice, thins slightly (1–2 mm), gradational, bottom: slightly scoured (1–2 mm)
14H-2, 129.3–130.2	0.9	123.19	3–5	NA–20	1–2	Orange silt (gray ~2 mm below surface); ~30% groundmass, bottom: slightly wavy
14H-2, 144–149†	5.0	113.34	5–10	0.5–60	NA	Tannish gray silt; ~3%–5% ooids; thinly laminated; top: planar, bottom: end of core
14H-5, 52.8–59*	6.2	116.93	≤5	(1–3)–(30–50)	1	Gray-tan silt; ~20% coated; top: partly scoured (filled with laminations), bottom: slight break, top concave, bottom slightly wavy
14H-5, 96.5–100	3.5	117.37	1–2	1–80	1	Cream-light gray silt, bottom tan (10%–15% biogenic), top: broken, wavy, bottom: slightly wavy
14H-5, 117.4–121.6*	4.2	117.57	1–3	1–(30–40)	<1	Gray-tan (orangish) silt, ~1 mm laminae at top
14H-5, 132.5–133.5	1.0	117.72	1–3	0.5–60	NA	Cream-tan silt, thins to the left, top: sharp, wavy, bottom: planar, broken
14H-6, 17.3–23*†	5.7	118.07	5–10	1–80	1–2	Brown silt, ~50% biogenic in bottom centimeter, top: concave, bottom: slightly wavy
14H-6, 23.5–26.5†	3.0	118.14	1–5→5–10	(1–15)→80	1	Gray-tan silt, sharp, top: slightly wavy, bottom: concave, pumice and biogenic increase in the bottom centimeters
16H-1, 36.5–43*	6.5	128.77	2–3	(2–3)–(15–25)	≤0.5	Gray silt, ~20% groundmass (~5% at bottom), top: slightly rippled
16H-1, 44–48*	4.0	128.84	1	2.5–20	<1	Gray silt, planar, bottom: gradational
16H-1, 60–64*	4.0	129.00	≤1	1.5–(20–30)	<1	Gray silt, gradational planar contacts
16H-1, 64.5–67*	2.5	129.05	≤3	2.5–50	≤1	Gray silt, top: wavy, bottom: planar
16H-1, 92–96	4.0	129.32	1–2	1.5–60	<1	Gray silt, top: planar, bottom: wavy
16H-1, 110.8–112	1.2	129.51	1–2	0.5–70	<1	Gray silt, light tan-light cream laminae
16H-1, 114–117.5	3.5	129.54	1–2	2.5–70	<1	Gray-light cream interlaminae, finely laminated, top and bottom: convex up
16H-1, 118.5–123*	4.5	129.59	1–2	2–70	<1	Gray silt, few discontinuous laminae
16H-1, 132–133	1.0	129.72	1–2	2–20	≤1	Gray silt, ~70% coated grains, top: planar, bottom: end of core
16H-2,12.5–16*	3.5	130.03	1–2	(1–1.5)–80	NA	Gray silt, tan, finely laminated, gradational convex up to the right
16H-2, 27.5–34*	6.5	130.18	1	2.5–(60–70)	<–0.5	Gray silt, one tan lamination (~1 mm) in center
16H-2, 118.5–124*	5.5	131.09	1–2	2–(60–70)	≤0.5	Gray silt, tan, finely laminated, ~3%–5% ooids
16H-3, 96–98.5*	2.5	132.35	1	0.5–(940–50)	NA	Tan silt, one brown lamination, ~5% ooids, top: sharp, bottom: gradational slightly wavy
16H-3, 110.5–114*	3.5	132.51	1–2	1–60	1–2	Tan finely laminated silt, bottom: gradational, both: slightly wavy
16H-3, 118–121.5*	3.5	132.58	1–2	1–15	<1	Tan silt, ~15% round pumice, top: convex up, bottom: rippled
16H-4, 27–40.5*	13.5	133.17	NA	1–30	1	Gray silt, ~15% round pumice, top: gradational, both: planar
16H-4, 40.5–42.5*†	2.0	133.31	20	5–30	≤1	Gray-tan finely laminated silt, biogenic ostracodes

Table T3 (continued).

Core, section, interval (cm)	Layer thickness (cm)	Depth (mbsf)	Biogenic	Glass – Pumice + 1	Roundness (Qz)	Description, structure, and contact
18H-1, 48–56.5*	8.5	147.88	1–3	2–60	≤0.5	Gray silt, gray-tan up to 51 cm (gradational), ~1% round pumice, ~5%–10% groundmass
18H-1, 62–67*	5.0	148.02	1–2	2–(70–80)	≤0.5	Gray silt, ~2%–3% round pumice, top: inclined, bottom: planar
18H-2, 5.8–9.5*	3.7	148.96	1–2	2–70	≤0.5	Gray-tan finely laminated silt, ~1% round pumice, top: convex at right side
18H-2, 50.5–57.5*	7.0	149.41	3	2–70	<0.5	Tan-brown silt, top half slightly laminated (54.5-gradational) lower half laminated, ~1% round pumice
18H-2, 79.7–89.2*	3.2	149.70	1–3	2–70	<0.5	Tan-brown finely laminated silt, ~1% round pumice, top: wavy, bottom: convex to right
18H-2, 88–90*	2.0	149.78	1–2	2–70	<0.5	Cream silt, ~1% round pumice, vesicular glass present, convex bed
18H-2, 112–115*	3.0	150.02	1–2	2–90	<0.5	Tan silt, ~3%–5% round pumice, top: slightly convex to right, bottom: end of core
18H-3, 95.5–97*	1.5	151.36	1–3	(1–1.5)–80	1–2	Gray-tan silt; ~1%–2% round pumice
18H-4, 0–3*	3.0	151.95	1–2	2–70	<0.5	Tan-gray silt, ~1% round pumice, some bioturbation, bottom: gradational planar
18H-4, 38–42*	4.0	152.28	1–2	2–70	<0.5	Tan silt, ~1% round pumice, top: wavy, bottom: planar
18H-4, 49–55*	6.0	152.35	1–3	2–70	<0.5	Tan and cream silt, ~1% round pumice, brown pod at top
18H-4, 83.5–88*	4.5	152.74	1–2	2–70	<0.5	Tan silt, ~1%–2% round pumice, top: slightly wavy, sharp, bottom: sharp planar and slightly bioturbated
Pleistocene						
201-1229A-						
1H-2, 99.6–99.9	0.3	2.50	≤3	2–3	NA	Gray silty crystal-pumice-hash, discontinuous, inclined lamina, top: gradational
3H-3, 50–50.5*†	0.5	17.90	10–15	75–NA	NA	Gray-white clay lamina, planar, top: gradational
5H-5, 126–129*	3.0	40.66	1–2	3–NA	1	White-cream silt, fines upward, slightly inclined and gradational contacts
6H-3, 18.7–20*†	1.3	43.09	5–10	2–5	NA	Gray-tan clay, slightly inclined, thins to one end
8H-3, 107–109*	1.8	69.97	0.5	<1–10	2–3	Gray silt, ~10%–25% dolomite, fines upward, inclined, top: gradational
8H-3, 108.8–109*	0.2	69.99	≤5	3–NA	1–2	Cream, crystal hash, very fine silt lamina, inclined
10H-5, 37–44*	7.0	85.77	3–5	(1–3)–NA	2–3	Gray clay, ~3%–5% dolomite, fines upward
11H-3, 2–6.5†	4.5	91.92	5–10	≤1	10–15	Gray-tan silt, ~3%–5% dolomite, fines upward
11H-3, 6.5–9.2*	2.7	91.97	1–3	(1–2)–10	1–2	Gray-tan silt, ~1%–3% dolomite, coated grains account for a majority of round grains
11H-3, 10.2	TL	92.00	1–3	(0.5–1)–NA	<1	Light-colored discontinuous silt lamina, ~20%–30% coated grains
11H-3, 39.3–39.6†	0.3	92.29	5–10	(1–2)–(5)	NA	Light-colored discontinuous silt lamina, ~3%–5% dolomite, bottom: gradational
11H-3, 49.5–50.5†	1.0	92.80	10–15	(2–3)–NA	NA	Light gray silt between gray clay beds, dolomite ~5%, 5%–10% opaques, normal grading
14H-1, 88.3–88.5†	0.2	118.28	1–3	<1–NA	NA	Cream silt, ~10%–15% dolomite, pinches out
14H-4, 139.2†	TL	123.29	5–10	<1–(10–15)	NA	Gray-tan-brown silty sand, slightly inclined
14H-5, 50–56*†	6.0	123.90	3–5	(2–3)–	≤1	Cream-gray-black silt, fines upward, ~10%–20% dolomite
18H-1, 0–3*	3.0	155.40	3–5	(1–2)–(15–20)	NA	Gray-tan silt, ~1%–2% dolomite
18H-1, 25–74†	49.0	155.65	5–10	(1–2)–(50–60)	NA	Gray-tan silt, two tan laminae-biogenic, fine-planar-laminae, bottom: inclined
18H-2, 115–115.5*	0.5	158.07	1–3	(1–2)–NA	NA	Gray-white-orange sandy silt lamina
18H-2, 117.2–117.4*	0.2	158.07	3–5	1–10	NA	Gray-white sandy silt lamina, bottom: gradational
18H-2, 117.4–127*	9.6	156.17	3–5	(1–2)–(10–15)	NA	Gray-tan silt, ~1%–2% dolomite, top: gradational
18H-3, 48–56*†	8.0	159.88	5–10	(1–2)–NA	NA	Gray-white poorly sorted feldspar-quartz silty sand within reworked bed, planar
18H-3, 114.5–122*†	7.5	159.55	10–15	1–(5–10)	NA	Gray-tan sandy silt, bottom: break
14H-5, 32–43.5	11.0	123.73	3–5	Too fine to tell	NA	Cream clay, ~5%–10%–15% dolomite, crystal-rich pods of dolomite, slightly concave contacts
14H-4, 18.5–23	4.5	122.08	≤10	(1–3)–NA	NA	Gray-cream clay, groundmass is first-order gray and white, discontinuous laminae and pod

Notes: Unless otherwise specified contacts between layers are planar and sharp. * = whole-rock geochemistry was acquired for these layers. † = layer is borderline primary (10%–15% biogenic material or dolomite). NA = not applicable; the feature was not observed. Glass–Pumice +1 percent = glass-coated grains, unless specified otherwise in the description. +2 = glass-coated grains are primarily round, ~20% of these are round pumice.

Table T4. Type 2, Type 3, and Type 4 ash layers. (**See table notes.** Continued on next page.)

Type 2 layers		Type 3 layers		Type 4 layers	
Core, section, interval (cm)	Age	Core, section, interval (cm)	Age	Core, section, interval (cm)	Age
201-1227A-		201-1227A-		201-1227A-	
2H-CC, 22.5–23	Pliocene	1H-2, 5.7	Holocene	1H-4, 56	Holocene
3H-1, 116–117.3	Pliocene	1H-2, 110.4	Pleistocene	4H-5, 73	Pliocene
		1H-4, 56	Pleistocene	4H-6, 29.3	Pliocene
		1H-4, 63	Pleistocene	4H-6, 87	Pliocene
		1H-4, 78	Pleistocene	5H-1, 14	Pliocene
		2H-1, 5.8	Pleistocene	6H-3, 135	Pliocene
		3H-1, 62.2	Pleistocene	6H-3, 137.3	Pliocene
		11H-1, 78.5	Miocene	7H-1, 14	Pliocene
		12H-1, 82.5	Miocene	7H-1, 150	Pliocene
				7H-2, 3	Miocene
				7H-2, 6	Miocene
				13H-3, 7–105	Miocene
201-1228A-		201-1228A-		201-1228A-	
1H-1, 98.5–99.3	Holocene	2H-4, 111.2–111.4	Pleistocene	5H-5, 134–150	Pleistocene
1H-1, 121.8–122.6	Holocene	2H-4, 131.7	Pleistocene	6H-1, 84	Pleistocene
1H-2, 7.8–8.3	Holocene	2H-4, 138.6	Pleistocene	7H-1, 27.5–31.7[†]	Pliocene
2H-3, 122.5–123.5	Pleistocene	2H-5, 28–30	Pleistocene	7H-3, 117–135	Pliocene
2H-6, 121.1–121.6	Pleistocene	2H-5, 29.8*	Pleistocene	7H-4, 10–14.8	Pliocene
3H-5, 121–124.5	Pleistocene	2H-7, 33.3–36	Pleistocene	7H-4, 126	Pliocene
3H-5, 35.3–38.3	Pleistocene	3H-3, 14–14.5	Pleistocene	8H-1, 123	Pliocene
3H-5, 106.8–107.4	Pleistocene	5H-2, 122–131	Pleistocene	9H-1, 62–70[†]	Pliocene
3H-5, 112.5–113.5	Pleistocene	6H-4, 4	Pleistocene	9H-1, 80.5–93.5[†]	Pliocene
3H-6, 149.3–150	Pleistocene	6H-4, 14–24	Pleistocene	9H-1, 73–78.5	Pliocene
3H-7, 0–2	Pleistocene	6H-4, 80	Pleistocene	9H-2, 112.7	Pliocene
4H-6, 84–85	Pleistocene	6H-6, 60	Pleistocene		
5H-2, 110–121.5	Pleistocene	Dispersed throughout the rest of this core.	Pliocene		
5H-2, 131–136	Pleistocene				
5H-5, 70–134	Pleistocene				
6H-1, 46	Pleistocene				
6H-1, 77.5–82	Pleistocene				
6H-4, 0–14	Pleistocene				
7H-1, 26–35	Pliocene				
7H-5, 84.5–87.2	Pliocene				
7H-6, 8-12	Pliocene				
7H-6, 136.5	Pliocene				
8H-1, 87.5	Pliocene				
8H-2, 23.8	Pliocene				
8H-5, 36	Pliocene				
8H-5, 41	Pliocene				
8H-5, 48.3	Pliocene				
8H-6, 81.5	Pliocene				
201-1229A-		201-1229A-		201-1229A-	
1H-2, 68–72.4	Holocene	1H-2, 98–99.6	Holocene	5H-4, 115–117	Pleistocene
2H-3, 117.2	Pleistocene	2H-6, 7–16	Pleistocene	6H-3, 26.2–28	Pleistocene
2H-5, 133–135	Pleistocene	2H-6, 77–80[‡]	Pleistocene	6H-3, 55–65	Pleistocene
2H-6, 0–7	Pleistocene	3H-6, 142–146	Pleistocene	10H-5, 44–52	Pleistocene
2H-6, 17.5–19*	Pleistocene	5H-6, 20–38	Pleistocene	10H-5, 52–59	Pleistocene
2H-6, 21.3–22.5*	Pleistocene	8H-1, 40–55	Pleistocene	11H-4, 28–33.5	Pleistocene
2H-6, 75.5–77	Pleistocene	8H-1, 86.5*	Pleistocene	11H-5, 85–87	Pleistocene
2H-7, 9–34	Pleistocene	8H-1, 83.5–84*	Pleistocene	11H-5, 124[†]	Pleistocene
3H-6, 83–88.8	Pleistocene	8H-2, 145–149	Pleistocene	13H-CC, 15–16	Pleistocene
5H-4, 71–77	Pleistocene	9H-4, 81–88[‡]	Pleistocene	14H-3, 111.8–112.4[†]	Pleistocene
8H-3, 111.5–113*	Pleistocene	12H-5, 43.5–56.5	Pleistocene	14H-4, 97–98	Pleistocene
9H-2, 104–114	Pleistocene	12H-6, 43.4–43.6	Pleistocene	14H-4, 98–104.5	Pleistocene
9H-2, 116–129	Pleistocene	14H-1, 42–56.5	Pleistocene	14H-4, 132(134)–137.5	Pleistocene
9H-2, 129–131.5	Pleistocene	14H-3, 126.5–134.5	Pleistocene	14H-5, 43.5–46.5[†]	Pleistocene
9H-2, 131.5–134	Pleistocene	14H-4, 68–78.5	Pleistocene	14H-5, 46.5–50	Pleistocene
9H-2, 134–136	Pleistocene	14H-4, 141.4–141.5	Pleistocene	14H-5, 56–60.5	Pleistocene
9H-4, 21–30	Pleistocene	14H-5, 116.5–122.5	Pleistocene	14H-5, 62.2–86.7	Pleistocene
9H-4, 51–53	Pleistocene	14H-CC, 20–32	Pleistocene	14H-5, 124–136	Pleistocene
9H-4, 58*	Pleistocene	18H-1, 97–100	Pliocene	14H-6, 68.5–72.6	Pliocene
9H-4, 65–66*	Pleistocene	18H-3, 6(4)–15	Pliocene	18H-2, 127–128.8	
9H-4, 68–72[‡]	Pleistocene	18H-3, 122–124	Pliocene		
9H-4, 88–92	Pleistocene				
9H-4, 110–115	Pleistocene				

Table T4 (continued).

Type 2 layers		Type 3 layers		Type 4 layers	
Core, section, interval (cm)	Age	Core, section, interval (cm)	Age	Core, section, interval (cm)	Age
9H-4, 111–111.5*	Pleistocene				
9H-4, 117.5–120	Pleistocene				
9H-4, 118.8*	Pleistocene				
10H-3, 40–41	Pleistocene				
11H-3, 2–6.5	Pleistocene				
11H-3, 30–32	Pleistocene				
11H-3, 39.3–39.6	Pleistocene				
11H-4, 0–7.5	Pleistocene				
11-4, 7.5–23.5	Pleistocene				
11-4, 73–75	Pleistocene				
11-4, 77.5–81	Pleistocene				
11-5, 63–66	Pleistocene				
11-5, 50–60	Pleistocene				
11-5, 132.5–134	Pleistocene				
11-5, 68.5–69	Pleistocene				
11-5, 69–85	Pleistocene				
11-5, 107.5–115.5	Pleistocene				
11-6, 0–3	Pleistocene				
11H-6, 5-9	Pleistocene				
11H-6, 9–11.3	Pleistocene				
11H-6, 11.3–11.5	Pleistocene				
11H-6, 13.5–15	Pleistocene				
11H-6, 15–16.5	Pleistocene				
11H-6, 29.5–35	Pleistocene				
11H-6, 39–40	Pleistocene				
11H-6, 40–42	Pleistocene				
11H-6, 114.1–114.3	Pleistocene				
12H-1, 116–126.5	Pleistocene				
12H-4, 31–34.5	Pleistocene				
14H-1, 85–88.2	Pleistocene				
14H-1, 120.5–124.5	Pleistocene				
14H-3, 108.5–111.8	Pleistocene				
14H-4, 48–49	Pleistocene				
14H-4, 78.5–86	Pleistocene				
14H-4, 139.5–141.4	Pleistocene				
14H-4, 146.5–150	Pleistocene				
14H-5, 0–19.5	Pleistocene				
14-5, 19.5–24	Pleistocene				
14-5, 25–27	Pleistocene				
14-5, 27–30.5**	Pleistocene				
14-5, 30.5–32.5**	Pleistocene				
14-5, 32.5–43.5**	Pleistocene				
14-5, 86.7–113.7	Pleistocene				
14-5, 122.5–123	Pleistocene				
14-6, 9.5–25	Pleistocene				
14-6, 30–33.5	Pleistocene				
14-6, 36–36.3	Pleistocene				
14-6, 58.9–68.5	Pleistocene				
14-6, 72.7	Pleistocene				
14-6, 93.5–95.2	Pliocene				
18-1, 74(78)–91(97)	Pliocene				
18-1, 98	Pliocene				
18-2, 116.5–117.2	Pliocene				
18-2, 128.8–130	Pliocene				
18-2, 137.8–138.5	Pliocene				
18-3, 1.2††	Pliocene				
18-3, 124–125	Pliocene				
18-3, 125–131.5	Pliocene				
18-3, 131.5–135	Pliocene				

Notes: Type 2 ash layers contain >20% and ≤60% biogenic material. Type 3 ash layers contain >60% biogenic material. * = pod, † = borderline (15%–20% biogenic material), ‡ = discontinuous, ** = clay (too fine grained to determine biogenic/volcanogenic components, †† =lens. Inclined layers have values in parentheses representing the centimeters to the lower depth of the contact.

Table T5. Average glass analyses.

Core, section, interval (cm)	Major element oxide (wt%)											
	SiO_2	Al_2O_3	FeO	MgO	TiO_2	P_2O_5	Na_2O	K_2O	CaO	MnO	S	Total
201-1227A-												
13H-2, 146–147.6	73.3	11.6	0.61	0.06	0.12	0.02	2.65	5.04	0.68	0.04	0.10	94.2
201-1228A-												
9H-1, 97–101.6	71.6	12.7	0.73	0.13	0.14	0.02	3.12	5.20	0.58	0.06	0.03	94.4
11H-2, 55–56.6	73.1	13.2	0.53	0.06	0.08	0.06	3.46	4.61	0.64	0.05	0.01	95.8
11H-2, 59–60.6	72.9	13.3	0.55	0.09	0.08	0.05	3.67	4.23	0.82	0.04	0.01	95.8
16H-3, 96–98.5	81.3	9.6	0.07	0.01	0.10	0.05	2.33	5.54	0.08	0.00	0.03	99.2
16H-4, 27–31.5	71.0	13.0	0.94	0.11	0.16	0.03	3.35	5.07	0.53	0.11	0.03	94.4
16H-4, 31.5–36	69.8	13.0	1.12	0.14	0.23	0.03	3.56	4.77	0.50	0.11	0.04	93.3
16H-4, 36–40.5	70.5	12.9	0.97	0.12	0.18	0.02	3.44	4.95	0.48	0.10	0.02	93.7
18H-2, 88–90	71.5	12.9	1.18	0.14	0.24	0.02	3.41	5.15	0.63	0.06	0.03	95.3
201-1229A-												
11H-3, 7–9	73.2	12.7	0.93	0.08	0.13	0.00	3.27	4.27	0.69	0.09	0.05	95.3
18H-1, 1–3	72.7	12.7	0.64	0.09	0.12	0.03	3.22	4.07	0.56	0.05	0.02	94.2
18H-1, 44.5–58	72.9	12.4	0.70	0.09	0.12	0.02	3.09	4.61	0.55	0.07	0.03	94.6
18H-2, 119–120.5	73.0	12.5	0.69	0.09	0.12	0.02	3.12	4.73	0.53	0.07	0.03	94.9
18H-3, 120–121.5	74.2	12.1	0.66	0.06	0.13	0.02	2.71	5.04	0.51	0.06	0.02	95.5

Table T6. Whole-rock geochemical analyses of Leg 201 Type 1 ash layers. (**See table notes.** Continued on next three pages.)

Core, section, interval (cm)	Major element oxides (wt%)										LOI (wt%)	Total (wt%)	Trace elements (ppm)			
	SiO$_2$	TiO$_2$	Al$_2$O$_3$	Fe$_2$O$_3$	MnO	MgO	CaO	Na$_2$O	K$_2$O	P$_2$O$_5$			Sc	V	Co	Ni
201-1227A-																
13H-2, 146–147.5*	63.9	0.31	15.4	1.96	0.03	0.45	3.03	4.29	3.07	0.1	7.2	99.8	2	39	1.90	<20
201-1228A-																
8H-3, 114–117	62.3	0.65	13.9	3.9	0.06	1.52	5.6	3.2	2.27	0.51	5.9	99.8	11	80	7.20	<20
9H1, 69.8–72	51.7	0.73	16.8	7.66	0.07	3.25	1.89	2.82	2.85	0.37	11.8	99.9	17	171	17.60	31.00
9H-1, 74.5–77	62.6	0.57	14.2	3.34	0.05	2	5.13	3.61	2.32	0.56	5.4	99.8	10	69	6.30	23.00
9H-1, 97–101.6	58.9	0.58	13.3	3.35	0.05	2.64	6.36	3.38	2.16	0.58	8.4	99.8	10	75	6.50	<20
9H-1, 121.4–124	59.8	0.59	13.4	3.35	0.05	2.49	6.26	3.44	2.18	0.65	7.6	99.9	10	72	6.40	<20
11H-2, 32.5–37.5	66.4	0.49	14.0	2.67	0.06	1.12	4.42	3.62	2.64	1.14	3.2	99.8	10	64	5.70	<20
11H-2, 50.2–52.3	58.8	0.56	14.4	4.71	0.07	1.78	2.05	3.75	3.12	0.42	10.2	99.9	10	106	14.80	40.00
11H-2, 55–56.6	60.7	0.44	13.9	3.95	0.05	1.21	4.64	3.81	2.86	1.75	6.5	99.9	11	69	8.50	29.00
11H-2, 59–60.6	69.2	0.23	14.9	1.65	0.04	0.61	1.83	4.42	3.78	0.12	3.0	99.9	4	21	1.70	<20
14H-2, 8.1–11.7	63.4	0.54	14.9	2.73	0.04	1.04	5.63	3.98	2.21	1.52	3.7	99.8	13	80	4.40	<20
14H-5, 52.8–59	63.7	0.64	15.3	3.03	0.04	1.19	4.64	3.93	2.25	0.81	4.3	99.9	13	101	4.40	<20
14H-5, 117.4–121.6	62.6	0.65	14.9	3.38	0.04	1.34	3.91	3.99	2.32	0.7	6.0	99.9	12	134	6.10	<20
14H-6, 17.3–23†	61.1	0.57	13.5	4.05	0.04	1.16	3.98	3.86	2.06	0.87	8.6	99.8	11	137	5.70	48.00
16H-1, 36.5–43	64.3	0.6	14.9	2.79	0.04	1.24	3.88	4.2	2.37	0.45	5.0	99.9	10	80	5.60	<20
16H-1, 44–48	62.7	0.61	14.7	2.74	0.05	1.3	5.02	4.12	2.3	1.2	5.0	99.9	16	85	5.20	<20
16H-1, 60–64	64.3	0.62	15.0	2.79	0.04	1.31	4.01	4.17	2.32	0.45	4.9	99.9	10	86	5.90	<20
16H-1, 64.5–67	63.0	0.6	14.8	2.73	0.05	1.29	4.79	4.15	2.33	1.06	5.0	99.9	14	83	5.30	20.00
16H-1, 118.5–123	64.3	0.61	15.1	2.81	0.04	1.27	3.97	4.25	2.41	0.43	4.6	99.9	11	92	5.50	<20
16H-2, 12.5–16	64.4	0.61	15.2	2.73	0.04	1.25	3.87	4.27	2.39	0.34	4.7	99.9	11	89	5.70	<20
16H-2, 27.5–34	64.4	0.63	15.0	2.87	0.04	1.29	3.75	4.17	2.43	0.38	4.8	99.9	11	94	5.80	<20
16H-2, 118.5–124	63.9	0.62	15.1	2.93	0.04	1.35	3.88	4.14	2.48	0.48	4.9	99.9	11	92	6.10	<20
16H-3, 87.8–89.2*	60.5	0.58	14.1	2.78	0.04	1.03	6.99	3.94	2.04	2.65	5.2	99.8	13	115	4.50	<20
16H-3, 96–98.5	61.7	0.59	14.2	2.8	0.04	1.05	6.41	3.94	2.1	2.19	4.8	99.9	12	112	4.80	<20
16H-3, 110.5–114	63.5	0.61	14.7	2.71	0.04	0.99	5.31	3.99	2.15	1.32	4.4	99.8	12	101	4.10	<20
16H-3, 118–121.5	62.5	0.58	14.5	2.66	0.04	1.08	5.53	4.09	2.19	1.57	5.0	99.9	12	103	4.30	28.00
16H-4, 27–40.5	61.5	0.66	14.4	2.94	0.05	1.24	6.43	4.03	2.08	1.81	4.4	99.6	13	80	5.10	32.00
16H-4, 40.5–42.5†	63.8	0.36	14.5	1.92	0.04	0.85	4.06	4.64	2.53	0.77	6.2	99.8	7	48	3.00	22.00
18H-1, 48–56.5	63.0	0.58	14.7	2.77	0.04	1.27	5.03	3.98	2.34	1.14	4.9	99.8	11	70	4.30	<20
18H-1, 62–67	61.8	0.59	14.6	2.8	0.05	1.34	5.39	3.95	2.28	1.37	5.4	99.6	12	75	5.60	<20
18H-2, 5.8–9.5	62.4	0.61	14.7	2.84	0.04	1.27	5.19	3.95	2.36	1.38	5.0	99.8	13	81	5.10	<20
18H-2, 50.5–57.5	63.0	0.58	14.7	2.87	0.04	1.28	4.66	3.99	2.45	1.06	5.0	99.7	12	77	4.70	28.00
18H-2, 79.7–82.9	62.4	0.59	14.6	2.95	0.04	1.32	4.68	4	2.47	0.97	5.6	99.7	12	81	4.90	<20
18H-2, 88–90	62.7	0.59	14.6	2.99	0.04	1.31	4.95	3.99	2.33	1.08	5.0	99.7	11	78	5.60	20.00
18H-2, 112–115	62.3	0.59	14.1	3.18	0.04	1.46	3.69	4.04	2.31	0.67	7.2	99.7	10	89	5.60	<20
18H-3, 95.5–97	60.3	0.56	14.1	2.71	0.05	1.15	6.55	3.87	2.23	2.19	5.8	99.6	13	82	4.10	29.00
18H-4, 0–3	63.2	0.59	14.7	2.9	0.04	1.23	4.5	4.05	2.44	0.93	5.1	99.8	11	74	4.70	<20
18H-4, 38–42	61.7	0.54	14.2	2.91	0.05	1.19	5.87	3.9	2.29	1.82	5.1	99.7	12	80	4.20	<20
18H-4, 49–55	62.9	0.57	14.6	3	0.05	1.27	4.63	4	2.38	0.99	5.3	99.8	11	74	5.50	35.00
18H-4, 83.5–88	61.3	0.57	14.2	2.94	0.05	1.2	6.54	3.82	2.18	2.12	4.6	99.6	14	76	4.50	<20

Table T6 (continued).

Core, section, interval (cm)	Major element oxides (wt%)										LOI (wt%)	Total (wt%)	Trace elements (ppm)			
	SiO$_2$	TiO$_2$	Al$_2$O$_3$	Fe$_2$O$_3$	MnO	MgO	CaO	Na$_2$O	K$_2$O	P$_2$O$_5$			Sc	V	Co	Ni
201-1229A-																
3H-3, 50–50.5[†]	51.9	0.7	16.3	7.02	0.07	2.8	1.92	2.68	2.57	0.14	13.6	99.7	18	166	17.00	50
5H-5, 126–129	58.9	0.7	15.1	5.87	0.07	2.47	3.1	3.33	2.53	0.18	7.2	99.5	18	116	13.70	25
6H-3, 18.7–20[†]	49.5	0.67	14.0	6.24	0.07	2.47	4.13	2.8	2.42	0.25	17.0	99.5	16	127	15.20	43
8H-3, 107–109	64.5	0.69	12.5	4.25	0.06	1.53	4.57	2.44	2.11	0.14	7.0	99.8	12	87	9.10	32
10H-5, 37–37	53.5	0.79	17.9	6.07	0.08	2.32	2.38	2.56	2.89	0.23	10.2	98.9	18	143	18.40	34
11H-3, 6.5–9.2	68.4	0.85	11.6	4.23	0.06	1.09	2.48	1.71	2.08	0.17	6.6	99.2	13	75	9.70	23
14H-5, 50–56[†]	62.5	0.65	13.3	4.31	0.07	1.72	4.98	3.13	2.21	0.26	6.4	99.5	14	93	12.20	31
18H-1, 0–3	60.9	0.55	13.1	3.19	0.05	1.53	6.53	3.59	2.25	1.8	6.2	99.7	12	83	5.90	24
18H-2, 115–115.5	60.0	0.6	13.4	3.41	0.05	1.42	5	4.16	2.25	0.76	8.0	99.1	12	86	6.10	24
18H-2, 117.2–117.4	61.7	0.63	14.0	3.28	0.06	1.35	5.37	3.86	2.34	1.22	5.8	99.5	14	84	5.90	21
18H-2, 117.4–127	61.5	0.59	13.9	3.41	0.05	1.35	4.52	3.97	2.22	0.73	7.4	99.7	12	79	6.90	28
18H-3, 48–56[†]	63.9	0.63	13.6	3.56	0.06	1.43	5.17	3.47	2.39	0.46	5.6	100.3	12	88	7.10	28
118H-3, 114.5–122[†]	62.3	0.57	14.0	3.04	0.06	1.23	5.65	4.02	2.2	1.36	5.0	99.4	13	76	6.20	24
14H-5, 32.5–43.5*	49.1	0.7	15.8	7.63	0.09	2.9	2.07	2.72	2.75	0.16	16.0	99.9	21	165	18.20	35
14H-4, 18.5–23*	49.5	0.68	16.3	7.86	0.08	2.74	1.45	2.65	2.67	0.07	15.8	99.8	20	226	19.60	36
201-1229C-																
1H-2, 92.5–94*	51.3	0.74	15.5	6.84	0.07	3.12	2.56	3.25	2.14	0.24	14.4	100.2	19	145	16.90	42
201-1229E-																
1H-2, 101–102.5*	60.9	0.67	14.1	5.07	0.07	2.19	4.38	3.24	2.12	0.22	7.0	100.0	16	110	10.90	25

Notes: Samples from Holes 1229C and 1229E were added late and do not appear in Table T3, p. 35. * = sample not part of ash layer described in Table T3, p. 35, † = borderline Type 1 (10%–15% biogenic matter or dolomite).

Table T6 (continued).

Core, section, interval (cm)	Rb	Sr	Y	Zr	Nb	Ba	La	Ce	Nd	Eu	Gd	Dy	Er	Yb	Th
							Trace elements (ppm)								
201-1227A-															
13H-2, 146–147.5*	101.9	745	5.7	132	6.0	822	26.4	46.1	19.1	0.70	1.49	0.96	0.45	0.51	10.3
201-1228A-															
8H-3, 114–117	82.8	384	26.0	161	8.8	495	26.3	53.4	24.8	1.1	4.67	3.78	2.41	2.49	8.2
9H1, 69.8–72	124.8	200	16.9	111	8.6	409	19.4	39.9	17.8	0.77	3.47	2.93	1.64	1.73	13.9
9H-1, 74.5–77	79.7	424	21.0	151	8.0	534	24.8	51.3	23.4	0.96	4.25	3.34	1.97	1.92	9.7
9H-1, 97–101.6	78.4	430	21.7	138	8.0	506	25.4	51.5	23.5	1.07	4.09	3.24	2.02	2	8.7
9H-1, 121.4–124	77.9	441	22.5	169	8.0	511	26.1	52.1	23.7	1.1	4.45	3.61	2.11	2.04	9.4
11H-2, 32.5–37.5	97.0	469	27.7	264	7.6	971	28.4	60.0	25.3	1.12	4.74	4	2.46	2.49	11.3
11H-2, 50.2–52.3	142.9	319	26.1	113	9.8	585	28.4	76.9	32.3	1.21	5.72	4.52	2.46	2.26	12.0
11H-2, 55–56.6	105.6	508	34.3	127	7.5	624	27.8	59.6	25.3	1.04	4.84	4.31	3.12	3.12	9.1
11H-2, 59–60.6	134.9	481	9.6	132	7.0	870	27.5	57.9	23.3	0.75	2.66	1.64	0.72	0.75	10.5
14H-2, 8.1–11.7	72.4	590	28.6	201	6.5	642	26.2	59.6	26.2	1.31	5.28	4.25	2.61	2.56	9.1
14H-5, 52.8–59	72.8	514	24.9	206	7.9	656	23.0	53.0	25.0	1.09	4.62	3.87	2.25	2.05	9.5
14H-5, 117.4–121.6	76.3	458	22.1	169	7.9	589	22.0	49.9	22.1	0.98	3.9	3.66	2.04	1.9	8.3
14H-6, 17.3–23†	68.5	416	26.1	189	6.9	527	23.3	54.2	26.0	1.04	4.89	3.77	2.18	2.14	10.3
16H-1, 36.5–43	75.6	428	20.2	162	7.3	609	22.7	48.2	22.3	1.08	4.01	3.26	1.9	1.77	8.3
16H-1, 44–48	75.4	543	27.0	187	7.9	605	26.9	55.8	27.0	1.27	5.17	3.96	2.56	2.42	10.6
16H-1, 60–64	79.8	463	21.7	177	8.1	597	24.5	52.6	23.6	1.13	4.21	3.45	1.99	1.89	8.4
16H-1, 64.5–67	78.6	505	24.9	173	7.5	617	26.8	54.3	24.4	1.14	4.38	3.71	2.31	2.08	8.5
16H-1, 118.5–123	81.2	447	21.2	159	8.1	613	25.2	52.1	23.3	1.08	4.08	3.36	1.89	1.82	8.7
16H-2, 12.5–16	80.4	448	20.4	158	8.2	622	24.2	49.6	22.7	1.13	3.98	3.28	1.89	1.81	8.3
16H-2, 27.5–34	80.4	424	19.5	155	8.1	656	23.8	49.0	22.9	1.03	4.37	3.08	1.76	1.85	9.3
16H-2, 118.5–124	84.2	454	21.4	157	8.3	622	25.4	52.7	23.7	1.14	3.92	3.26	1.93	1.84	9.1
16H-3, 87.8–89.2*	65.6	602	31.2	213	7.1	621	27.5	62.2	27.6	1.26	5.22	4.45	2.6	2.45	8.7
16H-3, 96–98.5	68.6	602	32.1	223	7.6	574	29.3	66.4	29.3	1.44	5.59	4.37	2.55	2.67	12.1
16H-3, 110.5–114	70.5	539	30.3	237	8.0	595	29.3	65.1	28.7	1.28	5.32	4.37	2.66	2.39	10.7
16H-3, 118–121.5	71.5	533	27.8	210	7.7	579	24.9	56.2	24.4	1.17	4.99	4.02	2.32	2.24	10.3
16H-4, 27–40.5	68.7	580	30.7	212	8.3	596	33.2	67.2	32.2	1.38	6.01	4.87	2.86	3.1	11.7
16H-4, 40.5–42.5†	86.9	434	18.1	120	6.8	619	25.0	50.2	22.1	1.08	3.59	2.92	1.74	1.88	8.5
18H-1, 48–56.5	77.0	478	24.2	153	7.7	764	25.5	50.8	24.7	1.11	4.19	3.72	2.27	2.12	9.8
18H-1, 62–67	80.8	532	27.6	182	8.0	609	28.8	58.9	28.1	1.34	5.17	4.14	2.24	2.34	11.5
18H-2, 5.8–9.5	82.7	531	27.9	189	8.0	596	29.7	59.4	28.4	1.26	5	4.1	2.38	2.61	10.1
18H-2, 50.5–57.5	85.1	479	23.9	152	8.3	597	26.7	51.8	24.6	1.13	4.83	3.7	1.94	2.19	10.2
18H-2, 79.7–82.9	87.8	487	25.2	162	8.3	605	28.5	56.5	25.5	1.18	4.58	3.98	2.08	2.04	10.8
18H-2, 88–90	80.4	500	27.3	178	7.9	612	30.2	59.3	29.0	1.38	5.32	4.17	2.51	2.54	10.1
18H-2, 112–115	85.3	419	21.2	152	8.1	578	25.1	49.7	23.4	1.02	4.12	3.07	1.94	2.01	11.0
18H-3, 95.5–97	76.0	579	29.0	188	7.6	586	28.9	58.2	27.6	1.17	4.98	3.82	2.53	2.67	11.0
18H-4, 0–3	86.4	473	24.0	165	8.3	601	27.9	54.2	26.3	1.14	4.36	3.66	2.2	2.18	10.3
18H-4, 38–42	79.0	538	27.7	173	7.7	572	29.8	58.9	27.8	1.25	5.08	3.98	2.17	2.45	11.5
18H-4, 49–55	83.8	465	24.5	184	7.8	582	28.7	56.2	28.1	1.22	4.99	3.57	2.23	2.31	11.3
18H-4, 83.5–88	75.9	567	31.2	223	8.1	562	34.1	68.3	30.3	1.45	5.74	4.66	2.56	2.78	12.7

Table T6 (continued).

Core, section, interval (cm)	Trace elements (ppm)														
	Rb	Sr	Y	Zr	Nb	Ba	La	Ce	Nd	Eu	Gd	Dy	Er	Yb	Th
201-1229A-															
3H-3, 50–50.5[†]	128.8	172	17.3	106	7.3	386	17.6	34.2	17.2	0.70	2.69	2.47	1.62	2.09	11.2
5H-5, 126–129	104.6	263	21.7	106	6.8	563	18.7	38.2	20.1	0.93	3.76	3.08	2.07	2.25	10.3
6H-3, 18.7–20[†]	108.1	233	20.6	129	7.9	418	20.2	41.0	20.6	0.88	3.45	3.09	1.93	2.23	13.0
8H-3, 107–109	83.2	241	24.5	247	11.5	321	27.1	55.6	23.7	1.02	4.18	3.79	2.43	2.55	11.4
10H-5, 37–37	114.5	216	27.9	164	12.2	400	33.6	71.9	33.0	1.56	5.28	4.70	2.89	2.99	13.3
11H-3, 6.5–9.2	82.7	163	36.2	378	15.3	303	30.7	65.1	30.1	1.31	5.83	5.49	3.58	3.38	10.4
14H-5, 50–56[†]	79.0	315	24.7	163	8.2	473	23.8	49.8	24.6	1.15	4.48	3.95	2.55	2.33	8.3
18H-1, 0–3	78.0	495	28.1	161	7.7	586	27.2	55.7	28.8	1.24	4.52	3.68	2.38	2.66	8.9
18H-2, 115–115.5	77.8	430	22.1	154	8.4	509	25.3	51.0	25.8	1.13	4.10	3.40	2.14	1.95	7.8
18H-2, 117.2–117.4	79.0	487	28.9	196	8.7	566	29.8	59.5	31.5	1.32	5.10	4.29	2.73	2.52	8.9
18H-2, 117.4–127	75.6	410	23.9	165	7.7	502	24.4	49.7	23.8	1.06	4.09	3.46	2.28	2.05	8.2
18H-3, 48–56[†]	80.0	382	25.9	234	8.5	516	26.1	52.8	28.5	1.20	4.31	4.32	2.53	2.54	9.8
118H-3, 114.5–122[†]	71.5	501	30.1	235	7.1	599	29.1	61.5	31.0	1.41	5.23	4.32	2.78	2.68	12.8
14H-5, 32.5–43.5*	117.4	178	19.4	107	8.1	329	21.7	44.4	21.7	0.92	3.99	3.23	2.02	1.88	10.9
14H-4, 18.5–23*	123.2	166	15.6	109	8.1	353	18.5	34.0	18.3	0.76	2.76	2.47	1.70	1.55	14.1
201-1229C-															
1H-2, 92.5–94*	104.4	177	22.0	97	8.5	377	18.9	40.4	19.6	0.86	3.94	3.54	2.37	2.25	11.4
201-1229E-															
1H-2, 101–102.5*	88.0	281	22.3	143	7.8	502	20.8	41.0	21.7	0.91	3.74	3.75	2.33	2.15	9.9